Aerodynamic Inverse Design of Airfoils in Two Dimensional Viscous Flows

Raja Ramamurthy

A Thesis

in

The Department

of

Mechanical and Industrial Engineering

Presented in Partial Fulfillment of the Requirements

for the Degree of Master of Applied Science (Mechanical Engineering) at

Concordia University

Montréal, Québec, Canada

November 2008

Your file Votre référence
ISBN: 978-0-494-63341-0
Our file Notre référence
ISBN: 978-0-494-63341-0

ABSTRACT

Aerodynamic Inverse Design of Airfoils in Two Dimensional Viscous Flows

Raja Ramamurthy

An aerodynamic inverse design method for viscous flow over airfoils is presented. In this approach, pressure distribution on the airfoil surfaces are prescribed as design target and the airfoil geometry is modified so as to reach the desired shape. In the design method, the walls are assumed to be moving with a virtual wall velocity that would balance the current momentum flux with the target pressure distribution; this virtual wall velocity drives the airfoil geometry to the shape that would produce the target pressure distribution where it would asymptotically vanish. This method was extended to address multi-point design and multi-element airfoils, and to use the pressure distribution of the airfoil suction surface as design variable. The approach is consistent with the viscous flow assumption and is incorporated into the governing equations which are expressed in an Arbitrary Lagrangian-Eulerian form, and are solved in a time accurate fashion. A cell-vertex finite volume scheme of the Jameson type is used for spacial discretization and time integration is performed by dual time stepping. Baldwin-Lomax turbulence model is used for turbulence closure. The validation of this approach is carried out for NACA 4-digit and 5-digit airfoils and RAE 2822 airfoil in transonic flow regime. The redesign cases include NACA 5-digit and 4-digit airfoils, the latter design experiencing large separation, RAE 2822 airfoil in transonic regime, multi-element airfoil and a dual-point design case.

ACKNOWLEDGEMENTS

I do not have enough words to express my gratitude to my professor Dr. Ghaly for offering me this opportunity, providing guidance, sharing his expertise and mentoring me in difficult situations. Thank you very much.

I extend my sincere gratitude and respects to my parents who have always done their best to see that I accomplish my dreams. For, it is them because of which I am here in the first place. I am also very much grateful to various members in the family especially my uncle and aunt, my cousin brother and sisters, whose guidance has been very valuable throughout the course of this journey.

The help from the staff of ENCS and for their continued support during my stay here in Concordia deserves special thanks. I am also thankful to the program advisors Ms. Leslie Hosein and Ms. Charlene Wald for all the help I have received from them.

I cannot finish without expressing my heartfelt appreciation to all my friends especially Benedikt Roidl, Mohammad Arabnia, Vadivel Kumaran, Sandeep Jella, Suresh Patra, Shahin and others of CFD Lab for for their support, valuable insights and many of the interesting discussions and also at times putting up with my irrational thoughts during the course of this work.

TABLE OF CONTENTS

LIST OF FIGURES

LIST OF TABLES

LIST OF SYMBOLS

c	Speed of sound
D	Dissipative and body force terms
e	Total energy
F	Convective flux vector, virtual momentum flux vector
G	Convective flux vector
H	Total enthalpy
i, j, k	Counter
M	Mach number
n	Normal vector
p	Pressure
Pr	Prandtl number
R	Gas constant, residual vector, Riemann Invariants
Re	Reynolds number
s	Wall displacement
T	Temperature
t	Fictitious or physical time
U	Primitive variable vector
u	Velocity in x-direction
v	Velocity in y-direction
L	Lift force
D	Drag force
c_l	Coefficient of lift
c_d	Coefficient of drag
ε	Under-relaxation factor for wall movement
Γ	Cell surface
τ	Stress tensor
λ	Stokes relation

δ	Kronecker delta, changes in characteristics
ρ	Density
γ	Specific heat ratio, damping coefficient
Ω	Control volume
μ	Dynamic viscosity

Subscripts

i	Extrapolated from interior domain
inf	Free stream conditions
F	Flux average value
0	Total quantity
new	Current fictitious time step
old	Previous fictitious time step
g	Grid contribution
b	Boundary values

Superscripts

$-$	Suction side
$+$	Pressure side
v	Virtual quantity
d	Design quantity

Acronyms

AOA	Angle of attack
Cp	Coefficient of pressure
CFL	Courant number
CFD	Computational fluid dynamics
LE	Leading edge
RANS	Reynolds number averaged Navier-Stokes
TE	Trailing edge
ALE	Arbitrary Lagrangian Eulerian
SCL	Space conservation law

Chapter 1

Introduction

Simulating viscous fluid flow using the Reynolds Averaged Navier Stokes (RANS) equations is now the most common tool for determining quantitatively the flow physics and properties in many industrial flow applications. One of the key interests in the aircraft industry is the performance of wings in flight and state of the art numerical simulations are now being used to analyze the designed planforms. With the advent of higher computing powers, designers can use Computational Fluid Dynamics (CFD) as a tool along with their experience, to design an airfoil that would provide optimal performance at specified flow condition(s). However, the design lead time will be too long, and the resulting performance will depend almost entirely on the designer's experience.

Today, there are design methodologies at the designer's disposal that can be used to improve the performance of a given wing or airfoil. The design trends are well detailed by Dulikravich [1]. One of the design methods being implemented is numerical optimization, where the airfoil geometry parameters are modified iteratively using an optimization method in order to satisfy certain objectives. Although optimization method is flexible in aspects of performing multi-objective and multi-disciplinary problems simultaneously and can be coupled with any kind of flow solver

to achieve a certain objective function(s), the implementation requires high computing resources to reach the target shape that would satisfy the specified objective function in a reasonable time. The other method that is being implemented is the adjoint method / control theory which is beneficial when optimizing a large number of design variables. However, the implementation also requires some initial number of analysis runs which again leads to utilization of computational resources. Also if the objective function contains multiple minima, then the adjoint approach based on gradient technique will converge to the nearest local minimum without searching for the global minimum. One of the direct approaches available to the designer is inverse design where the designer could provide a physical target pressure or Cp distribution and the inverse design method would provide an airfoil shape that satisfies the target. This is a one shot approach as the airfoil shape is driven by the difference between the available and target Cp distributions and the flow governing equations are modified in such a way that the corresponding shape and performance are obtained as part of the solution. This reduces both time and computing resources as compared to other design tools and the designer is sure to reach a final airfoil shape that would provide the desired performance. It is quite evident that the target distributions have to be physical, otherwise a solution may not be reached or may not be physical.

The main objective of this work is to develop an inverse aerodynamic design method suitable for external flow applications, starting from a recent inverse method that was developed for internal flow applications. The inverse method and the underlying CFD method are modified to accommodate external flow features, a new set of inverse design variables is introduced and inverse design in the context of dual or multi-point design is developed. The inverse method is first validated and then it is applied to several design cases that demonstrate the robustness, usefulness and flexibility of this method in designing different types of airfoils under different flow conditions.

1.1. Inverse design approach

1.1.1 Previous investigations

Two-dimensional inverse design method dates back several decades and has been under implementation for long as this was one of the first design tools that the designers developed. The method of obtaining an aerodynamic profile having a desired pressure distribution was first developed by Lighthill [2] wherein the incompressible potential flow equations were solved by conformally mapping a profile on a unit circle. This method was extended to compressible flow equations by McFadden [3]. Garabedian and Korn [4] used hodograph plane to design airfoils in transonic flows. The method of Tranen [5] uses the integrated surface velocities obtained from specified pressure distributions to obtain a surface potential and then potential flow equations are solved with a Dirichlet boundary condition. The geometry movement is determined from the computed normal velocity through the surface. The extension of this method to three dimensions was implemented by Henne [6]. Garabedian and McFadden [7] solved inverse problem in three dimensions where potential flow functions were solved using an artificial time-dependent equation and the airfoil surface is treated as a free boundary. This is not a comprehensive list of achievements in inverse design upto the early eighties wherein potential flow and (or) Euler equations were solved, it gives an outlook of the implementation of the inverse design method in time. The current review focusses on inverse methods that include viscous flow features as a part of the method and (or) the analysis.

Although the inverse method carried out in earlier stages [8], used Navier-Stokes equations for analysis, which would yield more accurate pressure distributions, there are traces of potential flow elements in the design problem. Even with the possibility of incorporation of boundary layer equations and the interaction coupling procedures

in the inverse design formulation, the implementation is effective in only cases of attached flows or flows with weak separation and shocks. The design code developed in [9] also incorporates full potential equations for the inverse methods along with boundary layer coupling. A full viscous inverse method has been implemented [10] where the difference in velocity distributions between the target and current is used to drive the airfoil geometry, the velocity being derived from potential flow equations. The PROFOIL code [11, 12, 13, 14, 15] which is a dedicated inverse tool has been developed based on conformal mapping and uses the panel method coupled with boundary-layer scheme to analyze the characteristics of resulting airfoils, the main ability of having the capability to perform multi-point design. Approach for multi-point design [16] following the Modified Garabedian-Mcfadden method has also been successful for the inverse design procedure. The method of Milholen [17] is a very detailed and effective approach, especially in the leading edge section as it is based on streamline curvature principles. As can be inferred from the above mentioned procedures wherein potential flow equations, Euler equations along with boundary layer coupling were solved, and even in cases of Navier-Stokes analysis, the results obtained would only be approximate in cases of Low Reynolds number flows, flows with considerable separation and flows with shocks where viscosity and compressibility effects have a significant impact on the solution.

1.1.2 Present implementation

The implementation presented in this work is consistent with the viscous flow assumption and the airfoil geometry moves with a virtual wall velocity that is computed from the balance of momentum fluxes that arise due to the difference between the current and target pressure distributions. The inverse method is incorporated into a time accurate solution of the Reynolds-averaged Navier-Stokes equations, expressed in an Arbitrary Lagrangian-Eulerian form to account for mesh movement. Daneshkhah

and Ghaly [18, 19, 20] implemented the design methodology for internal flow applications, and used it in the redesign of the VKI-LS89 transonic turbine vane [20]. In this work, the design method is developed for external flow application and is validated and applied to redesign airfoils in 2D viscous flow. The method is also extended to accommodate design of high lift devices and to address dual and multi-point design.

1.2. Flow analysis

The flow equations are solved in two dimensions using Reynolds-averaged Navier-Stokes (RANS) equations. The Baldwin-Lomax turbulence model [21], is adapted for unstructured meshes [22] for turbulence closure. The governing equations are discretized in space by second order cell-vertex finite volume method of Jameson's type on a fully unstructured triangular mesh [23]. An explicit Runge-Kutta time marching is carried out to obtain a steady state solution. Local time stepping and implicit residual smoothing are employed to ensure stability and convergence acceleration. Riemann invariants at far field boundaries and no slip condition at walls are employed as boundary conditions. For the inverse methodology, the governing equations are modified so as to incorporate movement of the wall and hence the deforming mesh. For this, Arbitrary Lagrangian-Eulerian (ALE) formulation is employed where the grid velocities due to the moving mesh is computed from the Space Conservation Law (SCL) [24]. A time accurate scheme using dual time stepping is implemented and marching in physical time is done after every design step.

1.3. Thesis outline

This memoire consists of five chapters including the introduction. The second chapter describes the numerical implementation giving the flow governing equations and the ALE formulation. Chapter three gives a detailed overview of the inverse design

formulation and its implementation along with different choices of design variables as well as general design considerations. Chapter four presents the validation of the design method for NACA 0012 and NACA 2412 airfoils and the application of the design method to redesign different airfoils. First, NACA 23012 airfoil has been redesigned to increase the L/D ratio. The second case investigates NACA 2412 airfoil at high angle of attack in the presence of massive flow separation. The third case is the redesign of RAE 2822 airfoil in transonic flow regime wherein the location of shock is moved in the downstream direction to reduce drag. The fourth case consists of redesign of a multi-element NLR airfoil. The final case is presented for a dual-point design where NACA 2412 airfoil has been redesigned to simultaneously satisfy target design profiles at two different operating points. The final chapter summarizes the main achievements and provides some recommendations for future work. The main text is followed by two appendices that complement the work. Appendix A gives the implementation of the time-accurate RANS equations using CFD and Appendix B presents a brief overview of the Baldwin-Lomax turbulence model.

Chapter 2

Numerical Implementation

In this chapter, the numerical implementation of the governing equations is presented. The governing equations are discretized using a cell-vertex finite volume approach and are solved in a time accurate manner using an Arbitrary Lagrangian-Eulerian (ALE) formulation. Baldwin-Lomax turbulence model was implemented for turbulence closure. It is to be noted that, although the numerical approach uses a time accurate method to design the airfoil, that solution corresponds to a target steady state pressure distribution that is reached asymptotically. Marching in physical time is done so as to eliminate any temporal errors that may arise due to the movement in airfoil geometry and also to increase the convergence rate of the design problem.

2.1. Governing equations

The fluid motion is described by the Reynolds-averaged Navier-Stokes (RANS) equations. The conservative form of the governing equations is written as

$$\frac{\partial U}{\partial t} + \frac{\partial (F - F_v)}{\partial x} + \frac{\partial (G - G_v)}{\partial y} = 0 \tag{2.1}$$

and with the inclusion of grid velocities, the governing equations take the form

$$\frac{\partial U}{\partial t} + \frac{\partial (F - F_g - F_v)}{\partial x} + \frac{\partial (G - G_g - G_v)}{\partial y} = 0 \tag{2.2}$$

where

$$U = \begin{bmatrix} \rho \\ \rho u \\ \rho v \\ \rho e \end{bmatrix}, \quad F = \begin{bmatrix} \rho u \\ \rho u^2 + p \\ \rho uv \\ \rho uH \end{bmatrix}, \quad G = \begin{bmatrix} \rho v \\ \rho uv \\ \rho v^2 + p \\ \rho vH \end{bmatrix} \tag{2.3}$$

$$F_g = \begin{bmatrix} \rho u_g \\ \rho u u_g \\ \rho v u_g \\ \rho e u_g \end{bmatrix}, \quad G_g = \begin{bmatrix} \rho v_g \\ \rho u v_g \\ \rho v v_g \\ \rho e v_g \end{bmatrix} \tag{2.4}$$

$$F_v = \begin{bmatrix} 0 \\ \tau_{xx} \\ \tau_{xy} \\ \tau_{xx} u + \tau_{xy} v + k \frac{\partial T}{\partial x} \end{bmatrix}, \quad G_v = \begin{bmatrix} 0 \\ \tau_{yx} \\ \tau_{yy} \\ \tau_{yx} u + \tau_{yy} v + k \frac{\partial T}{\partial y} \end{bmatrix} \tag{2.5}$$

$$p = (\gamma - 1)\rho \left[e - \frac{u^2 + v^2}{2} \right] \tag{2.6}$$

$$H = e + \frac{p}{\rho} \tag{2.7}$$

γ is the constant specific heat ratio assuming a perfect gas relation. By considering Newtonian Fluid defined by two viscosity coefficients λ and μ, the stresses are given as

$$\tau_{ij} = \mu(\partial_i \vec{V}_j + \partial_j \vec{V}_i) + \lambda(\delta_{ij}(\vec{\nabla} \cdot \vec{V})) \tag{2.8}$$

where μ represents the combination of both laminar (μ_l) and turbulent (μ_t) viscosities. The value of λ is taken from the Stokes relation $\lambda = -\frac{2}{3}\mu$.

The flow quantities are non dimensionalized with total pressure and/or temperature and the spacial variables with a reference length.

$$p = \frac{p}{p_0}, \quad T = \frac{T}{T_0}, \quad u = \frac{u}{\sqrt{RT_0}}, \quad v = \frac{v}{\sqrt{RT_0}}, \quad \rho = \frac{\rho}{p_0/RT_0}$$
$$x = \frac{x}{l_{ref}}, \quad y = \frac{y}{l_{ref}}, \quad t = \frac{t}{t_{ref}}, \quad \mu = \frac{\mu}{\mu_{ref}} \tag{2.9}$$

where l_{ref} is equal to the chord of the airfoil.

2.2. Boundary conditions

The two boundary conditions that are commonly used for the external flow around bodies are the wall and the far-field boundary conditions.

Far-field boundary

Far-field boundary conditions are the ones where the flow enters or leaves the computational domain. They are generally located far from the airfoil so that free stream conditions can be considered. The formulation implemented here is derived from the method of characteristics where Riemann invariants [25, 26, 27] are used to describe the flow, which are given as

$$R_1 = v_n + \frac{2c}{\gamma - 1} \tag{2.10}$$

$$R_2 = v_n - \frac{2c}{\gamma - 1} \tag{2.11}$$

where v_n is the velocity normal to the boundary surface and c is the speed of sound. Since this is a two dimensional case, the pressure p and the surface tangential velocity v_t are the third and fourth properties that describe the remaining acoustic waves.

Subsonic inflow

This condition corresponds to three incoming and one outgoing characteristic wave along the boundary. The outgoing wave is directly extrapolated from the interior of the domain while the three incoming waves are computed from the free stream conditions. Free stream pressure, surface tangential velocity and Eq. 2.10 are used to describe the incoming waves and Eq. 2.11 is taken as the outgoing wave, which are expressed as

$$R_{inf} = v_{n_{inf}} + \frac{2c_{inf}}{\gamma - 1} \tag{2.12}$$

$$R_i = v_{n_i} - \frac{2c_i}{\gamma - 1} \tag{2.13}$$

where subscript inf refers to the free stream conditions and i refers to the interior value. By adding and subtracting equations 2.12 and 2.13 we get

$$v_{n_b} = \frac{R_{inf} + R_i}{2} \tag{2.14}$$

$$c_b = (R_{inf} - R_i)\frac{\gamma - 1}{4} \tag{2.15}$$

where v_{n_b} and c_b refer to the surface normal velocity and speed of sound on the boundary itself. The remaining two characteristics are

$$v_{t_b} = v_{t_{inf}}, \quad p_b = p_{inf} \tag{2.16}$$

These three equations, namely 2.14 to 2.16, describe the boundary properties from which temperature, density and other properties are calculated.

Subsonic outflow

This condition corresponds to three outgoing and one incoming characteristic wave. Again the outgoing characteristics are directly extrapolated from the interior of the

domain and the incoming wave is taken from the free stream condition. Pressure, surface tangential velocity and Eq. 2.11 are used to describe the incoming waves and Eq. 2.10 is taken as the outgoing wave which are expressed as

$$R_{inf} = v_{n_{inf}} - \frac{2c_{inf}}{\gamma - 1} \tag{2.17}$$

$$R_i = v_{n_i} + \frac{2c_i}{\gamma - 1} \tag{2.18}$$

By using the methodology as described for subsonic inflow, the boundary properties are calculated.

Solid wall boundary

For steady state analysis, this condition is represented by using no slip condition meaning setting the velocities at the wall to zero. In case of moving wall the velocity at the wall becomes equal to the virtual velocity (described in Chapter 3).

2.3. Arbitrary Lagrangian-Eulerian formulation

Arbitrary Lagrangian-Eulerian (ALE) formulation is an approach to solving problems with moving boundaries and yet using the Euler frame of reference. This is useful for the analysis of flexible boundary and moving wall. The ALE differential form for the conservation equations are determined by replacing u and v in the convective terms with the relative velocity $(u - u_g, v - v_g)$. The modified equations are given as

$$\frac{\partial \rho}{\partial t} + (\vec{V} - \vec{V_g}).(\vec{\nabla}\rho) + \rho.(\vec{\nabla}\vec{V}) = 0 \tag{2.19}$$

$$\frac{\partial(\rho\vec{V})}{\partial t} + ((\vec{V} - \vec{V_g}).\vec{\nabla})(\rho\vec{V}) = \rho b - \vec{\nabla}p + \mu\nabla^2 V + \frac{\mu}{3}\vec{\nabla}(\vec{\nabla}.\vec{V}) \tag{2.20}$$

$$\frac{\partial(\rho e)}{\partial t} + ((\vec{V} - \vec{V_g}).\vec{\nabla})(\rho e) = -p(\vec{\nabla}.\vec{V}) + \vec{\nabla}.(k\vec{\nabla}T) + \phi \tag{2.21}$$

where b represents the body forces and ϕ represents mechanical energy dissipation. By substituting $v_g = 0$ we get the Eulerian formulation. In the ALE formulation, the nodes on the body move at the speed of deformation. The rest of the nodes move in an arbitrary fashion to incorporate the wall movement but in a way such that mesh crisscrossing does not occur and the space conservation law is respected.

2.4. Space conservation law

The movement of the coordinate system results in additional conservation equation that needs to be satisfied simultaneously. The law follows the principle that the integral $V_g.nd\Gamma$ equals the volume change of the control volume. For a uniform flow with zero velocity, the integral form of the continuity results in the Space Conservation Law (SCL) equation:

$$\frac{d}{dt}\int\int_{\Omega} d\Omega + \oint_{\Gamma} \vec{V_g}.nd\Gamma = 0 \tag{2.22}$$

where $V_g = (u_g, v_g)$ is the cell face velocity, $n = (n_x, n_y)$ is the cell face normal vector, Ω is the control volume and Γ is the control surface. Not respecting the above relation leads to artificial sources and sinks leading to instabilities [24].

2.5. Additional driving terms

From discretizing the mass conservation equation using the ALE formulation, additional source term arises which is expressed as

$$\Delta\rho = \sum_{k}[\rho\vec{V}.n - (\rho\vec{V_g}.n + \rho\frac{\Delta\Omega}{\Delta t})]\frac{\Delta t}{\Omega} \tag{2.23}$$

The first term in the right hand side of Eq. 2.23 is the residual for a fixed mesh. The second and third additional terms are obtained due to mesh movement. The convective fluxes must be measured by subtracting the mesh velocity from the fluid velocity. The convective fluxes entering the control volume cause a variation of mass in the control volume, which is the product of $density \times volume$.

In the inverse method, the two additional terms converge to zero as steady state is reached. It could be concluded from this that the presence of those terms is not necessary for steady computations, as proposed by Demirdzic and Peric [24]. However, experience has shown that these additional terms are essential for obtaining a satisfying convergence rate of the computations at transonic flow conditions with shocks [28, 29].

Chapter 3

Inverse Design Methodology

In this section, the inverse design methodology is detailed. The method follows the principle that as long as there is a pressure difference existing between the target and current pressures, the airfoil moves with a virtual velocity that tends to zero as the difference approaches zero. This virtual velocity that drives the airfoil shape to the one which would produce the target pressure, is proportional to the pressure difference and is derived from a balance of momentum fluxes on the airfoil surface. The implemented scheme is a time accurate solution of the RANS equations wherein the governing equations are solved in Arbitrary Lagrangian-Eulerian (ALE) formulation so as to take into account the movement of the airfoil and hence the deformation of the mesh. The target performance is prescribed by specifying the target pressures on the pressure and suction surfaces or suction pressure and thickness distributions.

3.1. Inverse design formulation

In the inverse methodology formulated by Daneshkhah and Ghaly [18], the airfoil virtual velocity distribution $\mathbf{v} = (u^v, v^v)$ is derived from the momentum flux balance between the target pressure distribution on a fixed airfoil and current pressure distribution on an airfoil with moving walls. When the airfoil is moving with a virtual

velocity, the momentum flux in the Navier Stokes equations takes the form

$$\mathbf{F} = \begin{bmatrix} (\rho u^v u^v + p)\, n_x + (\rho u^v v^v)\, n_y \\ (\rho u^v v^v)\, n_x + (\rho v^v v^v + p)\, n_y \end{bmatrix} \tag{3.1}$$

where $\mathbf{n} = (n_x, n_y)$ is the vector normal to the airfoil surfaces. The virtual velocities are computed by equating the momentum flux on the moving wall with that prevailing at the target state. This is the state where the airfoil has the shape that corresponds to the target pressure distribution and hence the virtual velocities asymptotically reach zero and thereby the target momentum flux yields

$$\mathbf{F^d} = \begin{bmatrix} (p^d n_x) \\ (p^d n_y) \end{bmatrix} \tag{3.2}$$

By equating the above two fluxes Eq. 3.1 and Eq. 3.2, the virtual velocity components in x and y directions are found.

$$\begin{aligned} v^v &= \pm \left(\frac{n_y^2}{n_x^2 + n_y^2} \frac{|p^d - p|}{\rho} \right)^{\frac{1}{2}} \\ u^v &= v^v \frac{n_x}{n_y} \end{aligned} \tag{3.3}$$

The signs of the virtual velocities are chosen such that positive virtual velocities exist when there is positive pressure difference between target and current pressures and vice versa. Then the virtual wall velocity in the direction normal to the wall is computed as

$$v_n^v = \mathbf{v}^v \cdot \mathbf{n} \tag{3.4}$$

It is required that the virtual velocities computed be heavily under-relaxed so as to ensure the stability of the problem. This is expressed as

$$\omega = \varepsilon \cdot (1/c) \sqrt{|\Delta p|/\rho} \tag{3.5}$$

where $c$is the speed of sound and ε is a constant whose suggested value falls between 0.1 - 0.2 for subsonic cases and about 0.05 for transonic cases.

The wall displacement δs is proportional to v_n^v, but is in the opposite direction so as to counter this virtual velocity and thereby driving it to zero. Therefore δs is given as,

$$\delta s = -\omega \, v_n^v \, \delta t \tag{3.6}$$

where ω is the relaxation factor obtained from stability criterion and δt is the user defined physical time step. The airfoil shape is modified by adding δs to the current shape. The airfoil movement is represented schematically in Fig. 3.1. The resulting airfoil is scaled back to the original chord length. The new camberline is now computed from the modified geometry and in order to have a smooth profile, it is recommended to smooth the camberline by applying the following elliptic form.

$$f_j = f_j + \omega_s[|f_{j+1} - f_j|(f_{j+1} - f_j) + |f_{j-1} - f_j|(f_{j-1} - f_j)] \tag{3.7}$$

where j refers to the discrete points on the airfoil camberline. A typical value for the smoothing coefficient ω_s is 0.2 for subsonic case. It is also recommended to modify the smoothing coefficient with the amount of displacement δs. For generating new suction and pressure surfaces for cases having design variables as p^- and thickness distribution, the prescribed thickness distribution is now applied to the new camberline as follows:

$$f(x)_{new} = f(x)_{old} \pm 0.5(\delta s^+ + \delta s^-) \tag{3.8}$$

$$y(x)_{new}^{\pm} = f(x)_{new} \pm 0.5T(x) \tag{3.9}$$

In the case of p^+ and p^- design case, the thickness distribution is smoothed in a similar manner before computing the camberline so as to ensure a smooth profile, and depending upon the case, camberline smoothing may be avoided. After the new

geometry is obtained, the design constraints are enforced, as detailed in the next section, to get the final shape.

The next step is to displace the computational grid according to the wall movement. In the present implementation, this is done by using transfinite interpolation as it has the ability to displace the grid at a relatively low computational cost. The grid movement is represented in Fig. 3.2. From this grid movement, the grid velocities are calculated using the Space Conversation Laws (SCL) which is in turn substituted into the flow governing equations [30].

It is interesting to note that the present inverse formulation works well for inviscid as well as viscous flows although, in Eqs. 3.1 and 3.2, the viscous terms were neglected, and the balance of convective terms only was used to move the wall towards a shape that satisfies the target pressure distribution [29]. It is believed that this is due to the fact that all the studied cases correspond to high Reynolds number flows where the drag coefficient is about two order of magnitudes smaller than the lift coefficient.

3.2. Design constraints

A completely arbitrary choice of target pressure distribution does not necessarily mean that the inverse design problem is well posed. As described by Mangler [31], Lighthill [2] and later on by Volpe *et al.* [32], there are three integral constraints relating target pressures and free stream conditions that need to be satisfied to ensure a well posed problem. Otherwise, we may end up with a trailing edge crossover or an open airfoil or in any unrealistic configuration. In the present implementation this is taken care of by solving the inverse problem between 0.5% to 2% and 98% to 99.5% of the chord while the remaining parts fall near the leading and trailing edges are solved in analysis mode. To ensure the profile smoothness at the transition points, the slope of

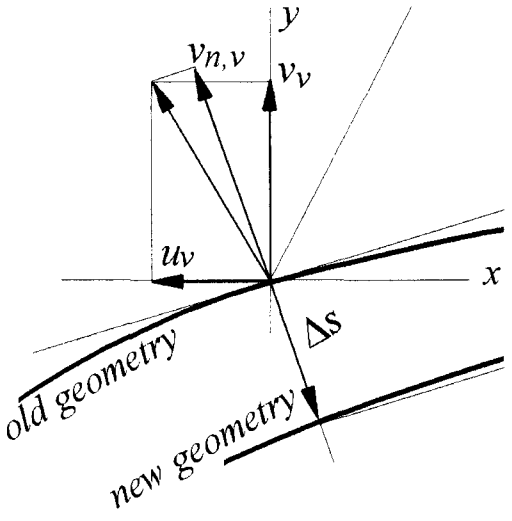

Figure 3.1: Schematic representation of wall movement

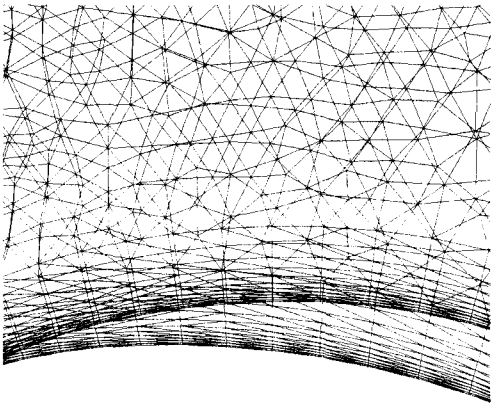

Figure 3.2: Schematic representation of grid movement

the camberline and the airfoil thickness are matched with those prevailing from the design region.

3.3. Design variables

In external flow, it is easier to follow the non-dimensional pressure coefficient (Cp) curve for performance which directly relates to pressure distributions on pressure and suction surfaces. Given a pressure distribution at a design point, an experienced aerodynamicist can vary the pressure distribution on the airfoil surfaces so as to get a prescribed performance (for e.g. increase in lift coefficient). This new pressure distribution is given to the inverse module as target pressures. The present implementation allows the designer to get the airfoil shape that corresponds to the prescribed pressure distributions.

There are different choices of design variables available to the designer to work with and the remaining flow variables are calculated as a part of the inverse design solution

Case 1: Pressure distribution on the airfoil suction and pressure surfaces

In this choice of design variables, the designer prescribes the pressures on both the suction and pressure surfaces. The difference between the target and the current pressure distribution is then used to compute the wall virtual velocities. This approach works very well from an aerodynamics view point, however, special attention should be given to the thickness distribution which is left as a part of the solution and thereby could pose a problem from a structural design point of view.

Case 2: Pressure difference across airfoil surfaces and its thickness distribution

The second choice of design variables developed by Daneshkhah and Ghaly [18] that is available to the designer is to specify the pressure difference between the pressure and suction surfaces $\triangle p_d$ and the airfoil thickness distribution. Translation of the pressure difference to the target pressure distribution on pressure and suction surfaces is done as follows

$$\begin{aligned} p_{avg} &= \frac{1}{2}(p^+ + p^-) \\ p_d^+ &= p_{avg} + \frac{1}{2}\triangle p_d \\ p_d^- &= p_{avg} - \frac{1}{2}\triangle p_d \end{aligned} \tag{3.10}$$

where $p^{\pm}$ are pressure distributions obtained from time-accurate solution during the design process. In some cases Eq. 3.10 may result in a non-physical value ($p_d^+ > 1$) during the design process. In such cases the target pressure distributions can be taken as follows, given the fact that the pressure distribution on pressure side is less sensitive to changes in geometry.

$$\begin{aligned} p_d^+ &= p^+ \\ p_d^- &= p^+ - \triangle p_d \end{aligned} \tag{3.11}$$

Case 3: Airfoil suction surface pressure and thickness distributions

A new choice of design variables implemented in this work is prescribing the suction surface pressure distribution along with the thickness distribution. The suction side

pressure is chosen here as the primary design variable as this surface predominantly dictates the performance of the airfoil. Also working with this surface pressure, gives more control on the flow over the airfoil such as weakening of a shock or reducing a flow separation region, which can result in a performance improvement. Since, not much of a change is expected on the pressure surface, the pressure from the analysis step is used as the target pressure. This means that no virtual velocities exist on the pressure surface and hence *no* design is being done, thereby keeping the number of design variables constant.

3.4. Inverse design algorithm

The inverse design algorithm is shown in Fig. 3.3. The inverse design module starts from a semi-converged or a fully converged solution on an initial geometry where the target pressures are read. The difference between the target and the current design pressures are used to compute the virtual velocities Eq. 3.3 (which exist at the first design step) which in turn are translated into displacements Eq. 3.6 that modify the airfoil geometry. The next step is to adjust the computational grid using transfinite interpolation. The grid velocities are then computed from space conservation law [24] Eq. 2.22. The grid velocities are added on to the governing equations and the analysis module is executed until the residuals reach a certain convergence level. In the analysis module unsteady RANS equations are solved in ALE form. The design and target pressures are compared and the whole process is repeated until the L_2 norm of the grid displacements are decreased to the tolerance values which ensures that the airfoil is not moving and steady state condition is asymptotically reached.

3.5. Dual and multi-point inverse design algorithm

The inverse design methodology started with the sole purpose of improving the airfoil performance at a prescribed design condition (for e.g. cruise condition). Often it is noticed that this improvement is achieved at the cost of reduced performance at other flow conditions, say off-design conditions. To bridge the gap between the two, an effort was made to take the concept of design process one step further and a new multi-point inverse design concept is developed.

For a description of the dual point design procedure, an airfoil geometry is analyzed at two target design conditions. Then, two target Cp distributions are given, due to which two virtual velocity distributions in each x and y directions are obtained namely u_1^v, v_1^v, u_2^v and v_2^v,. Both of these distributions are merged into one by providing weight w_1 and $w_2 = 1 - w_1$ for each design condition (for example, if improvement needs to be concentrated at design condition one, then a higher value of weight is assigned to condition one) as shown below.

$$u_w^v = w_1 * u_1^v + w_2 * u_2^v \tag{3.12}$$

$$v_w^v = w_1 * v_1^v + w_2 * v_2^v \tag{3.13}$$

Using the above weighted virtual velocity distributions, the airfoil geometry is modified and is analyzed again to get revised Cp distributions at the two specified design conditions. The whole process is repeated till the L_2 norm of grid displacements goes down to the prescribed tolerance value. It should be noted that since a weighted wall velocity approach is used, the design distributions may not always fall on top of the target. A flow chart for this process is given in Fig. 3.4.

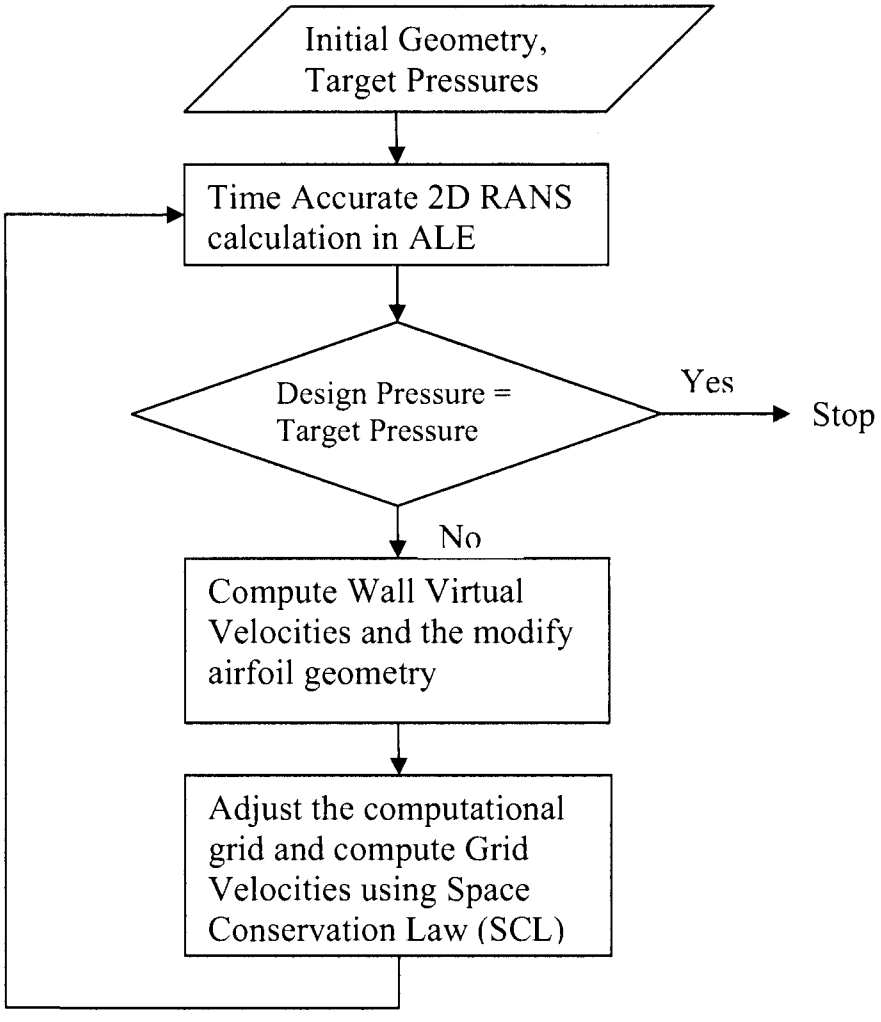

Figure 3.3: Computation algorithm for inverse design

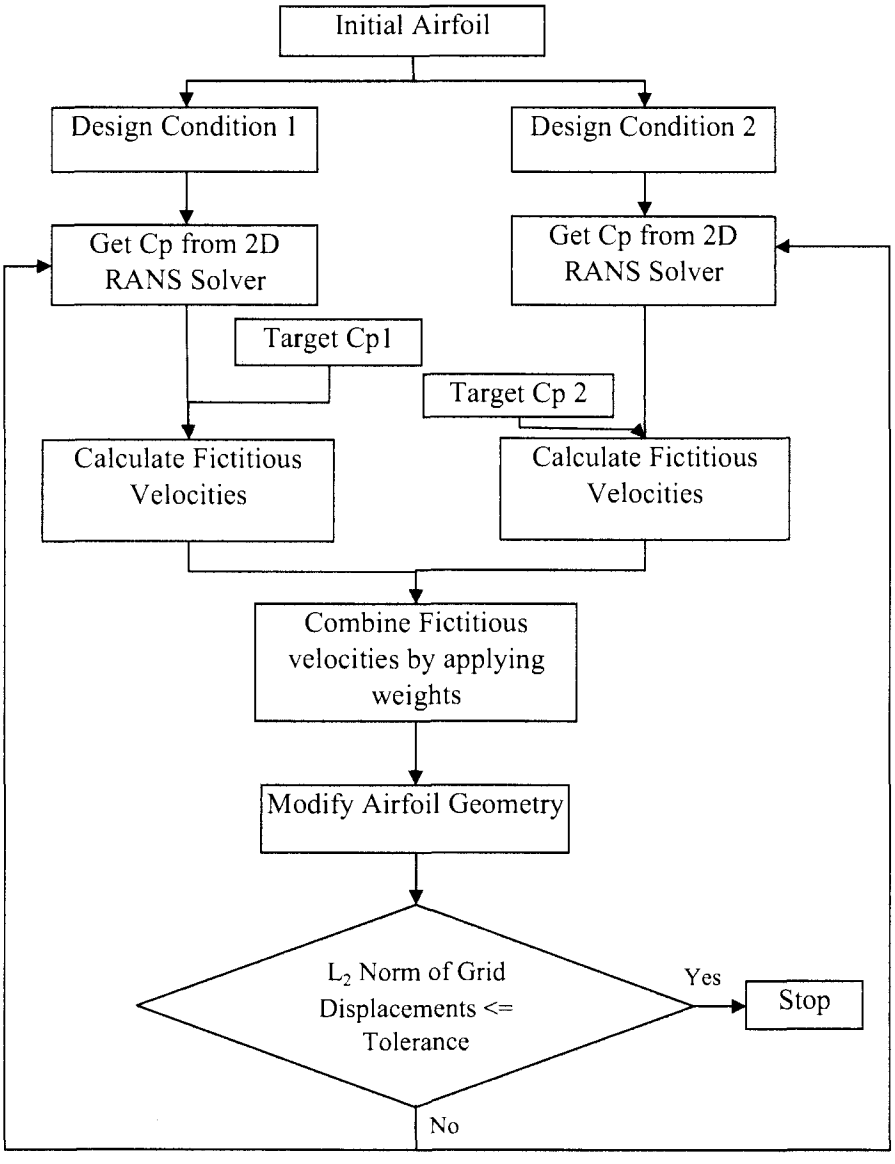

Figure 3.4: Flow chart for Dual point Design

Chapter 4

Validation and Redesign Cases

In this chapter validation of the inverse design methodology and its application to the redesign of airfoils are presented. These redesign cases are NACA 23012 airfoil to improve performance, NACA 2412 airfoil to reduce separation at a relatively high angle of attack to show the capability and the robustness of the method, RAE 2822 airfoil in transonic flow conditions and the redesign of a multi-element airfoil. Finally, the implementation was also modified to accommodate multi-point design, and was demonstrated on a NACA 2412 airfoil. These test cases show the ability of the inverse method to accomplish different tasks efficiently and accurately.

4.1. Inverse design validation

In this section, the inverse design methodology is validated for a NACA 4-digit airfoil.

Initially NACA 2412 and 0012 airfoils are analyzed at Mach number of 0.52 and angle of attack (AOA) of 4°. The NACA 4 digit airfoils have a finite thickness at the trailing edge. However the present calculations are carried out on a sharp edge airfoil that is obtained by extrapolating the thickness profile until a sharp trailing edge is reached and the the airfoil is then re-scaled to have a prescribed maximum thickness and chord of one. The numerical and experimental values [33] of the lift and drag

Table 4.1: Computed Values Vs Experimental Values for NACA 0012 airfoil, $M_{inf} = 0.5, AOA = 4°, Re = 2$ millions

Lift coefficient (c_l)		Drag coefficient (c_d)	
Computed	Experimental	Computed	Experimental
0.445	0.458	0.0096	0.0113

Table 4.2: Design Values Vs Target Values for Validation Case 1: NACA 0012 to NACA 2412, $M_{inf} = 0.5, AOA = 4°, Re = 2$ millions

Lift coefficient (c_l)		Drag coefficient (c_d)	
Design	Target	Design	Target
0.650	0.669	0.0105	0.0106

coefficients for NACA 0012 airfoil are given in Table 4.1.

To validate the inverse design, NACA 2412 airfoil was analyzed at the same conditions, and the pressure distributions calculated on the suction and pressure sides are prescribed as target and the initial airfoil shape is that of the NACA 0012 airfoil. The inverse design was started from the fully converged solution of NACA 0012 airfoil and the target Cp distribution was achieved in about 600 design steps. The L_2-norm of the grid displacements went down to 10^{-4} which indicated that the airfoil has reached the shape that corresponds to the prescribed pressure distribution. After every physical time step, the geometry is modified and the solution of the stationary problem is converged to 10^{-6}, which was achieved in around 200 pseudo-time steps. Figures 4.1 and 4.2 present the initial, target and design airfoil geometry and pressure distributions, respectively, where it can be seen that the NACA 2412 profile as well as the Cps are matched rather well. The design value of c_l and c_d compared with the target ones is given in Table 4.2.

The second validation case was carried out using the suction surface pressure distribution and thickness distribution as design variables (design case 3 in Chapter 3). AGARD AR 138 test case 1 [34] is chosen. NACA 0012 is analyzed at 11.74°

Table 4.3: Computed Values Vs Experimental Values for NACA 0012 airfoil, $M_{inf} = 0.299, AOA = 11.74°, Re = 1.86$ millions

Lift coefficient (c_l)		Drag coefficient (c_d)	
Computed	Experimental	Computed	Experimental
1.088	1.075	0.0386	0.0200

Table 4.4: Design Values Vs Target Values for Validation Case 2: NACA 0012 to NACA 23012, $M_{inf} = 0.299, AOA = 11.74°, Re = 1.86$ millions

Lift coefficient (c_l)		Drag coefficient (c_d)	
Design	Target	Design	Target
1.22	1.25	0.0321	0.0323

angle of attack, a Mach number of 0.299 and a Reynolds number of 1.86 millions. The c_l and c_d computed against the experimental values are given in Table 4.3. The lack of agreement in the value of drag coefficient is due to large separation at the trailing edge section which cannot be properly accounted for in the Baldwin-Lomax turbulence model. The suction side Cp distribution along with thickness distribution of NACA 23012 airfoil analyzed under the same conditions are prescribed on the fully converged solution of NACA 0012 airfoil and the target Cp was achieved in about 750 design steps. All other inverse design parameters were the same as that of the previous case. Figures 4.3 and 4.4 show the initial, target and design airfoil geometry and Cp distributions respectively. The comparison of values between the design and target are given in Table 4.4.

The third validation case is is that of a transonic flow over the RAE 2822 airfoil which has been analyzed at Mach no. = 0.725, AOA = 2.92°, Re = 6.5 millions, see AGARD AR 138 section A-6, test case 6. For this upstream Mach number, there is a transonic bubble on the suction side and a shock has been observed between 50 and 60 percent chord. The computed lift and drag coefficients are compared with the experimental values in Table 4.5. For the inverse design process, NACA 0012 airfoil

Table 4.5: Computed Values Vs Experimental Values for RAE 2822 airfoil, $M_{inf} = 0.725, AOA = 2.92°, Re = 6.5$ millions

Lift coefficient (c_l)		Drag coefficient (c_d)	
Computed	Experimental	Computed	Experimental
0.782	0.743	0.0111	0.0127

Table 4.6: Design Values Vs Target Values for Validation Case 3: RAE 2822 to NACA 0012, $M_{inf} = 0.725, AOA = 2.92°, Re = 6.5$ millions

Lift coefficient (c_l)		Drag coefficient (c_d)	
Design	Target	Design	Target
0.466	0.444	0.01644	0.01340

was analyzed under the same flow conditions and the pressure distribution obtained was chosen as the target distribution where a shock appears on the suction side and is located between 30 and 40 percent chord. Inverse design was started from a fully converged solution of RAE 2822 airfoil and the pressure distributions on pressure and suction surfaces of NACA 0012 were applied as target. The final airfoil shape corresponding to NACA 0012 was achieved in around 1200 design steps where the L_2 norm of grid displacements went down to $2\text{x}10^{-4}$. The number of design iterations is high when compared to the subsonic flow cases as the under-relaxation factors were kept low in order to maintain the stability of the problem and to eliminate any waviness that may occur in the shock region. Figures 4.5 and 4.6 show the initial, target and design airfoil geometries and Cp distributions respectively. The design values of c_l and c_d are compared with the target values in Table 4.6; given that this is a transonic case, the agreement is rather fair.

Based on the above validation results, the inverse method is applied to the redesign of several airfoils in the following sections.

Table 4.7: Redesign of NACA 23012 airfoil: $M_{inf} = 0.52, AOA = 4°, Re = 2$ millions

Lift coefficient (c_l)		Drag coefficient (c_d)		Lift/Drag (c_l/c_d)	
Design	Original	Design	Original	Design	Original
0.710	0.602	0.0118	0.0109	59.839	55.229

4.2. Redesign of NACA 23012

NACA five digit airfoil 23012 was chosen as a redesign case and it was analyzed at free stream conditions of AOA of 4°, Mach number of 0.52 and Reynolds number of 2 millions. The objective of the redesign is to increase the L/D ratio. The suction surface pressure and thickness distributions were prescribed as design targets. The flow over the NACA 23012 airfoil was simulated and was used to start the inverse design process. The target suction surface Cp was reduced between 10 percent and 60 percent. Care was also taken such that the target Cp had the same peak near the leading edge so that the pressure recovery would be similar to the original airfoil.

The target Cp was reached in about 550 design steps and the initial, target and design Cp distributions are shown in Fig. 4.7. The initial c_l was computed as 0.602 and the c_l obtained for the redesign airfoil was 0.710. This increase of lift coefficient can be attributed to the increase of camber of the designed airfoil. The c_l and c_d values in comparison with the original NACA 23012 airfoil are given in Table 4.7 The initial and design airfoil geometry are shown in Fig. 4.8.

4.3. Redesign of NACA 2412

The main aim of this redesign case is to apply the inverse method to a separated flow case in an attempt to reduce the separated flow region. NACA 2412 was analyzed at an AOA of 12°, Mach of 0.39 and Reynolds number of 2 millions. Target Cp was chosen such that the flow possesses higher energy upstream of the separation region

Table 4.8: Redesign of NACA 2412 airfoil: $M_{inf} = 0.39, AOA = 12°, Re = 2$ millions

Lift coefficient (c_l)		Drag coefficient (c_d)		Lift/Drag (c_l/c_d)	
*D*esign	Original	Design	Original	Design	Original
1.392	1.250	0.0437	0.0517	31.805	24.158

so as to energize the low momentum fluid near the wall and reduce the separation region, hence increasing c_l. Also the peak of the target Cp near the leading edge was reduced in magnitude thereby reducing the pressure recovery and hence delaying separation. Reduction of peak Cp also leads to lower mach numbers, and transonic flow or a weak shock near the leading edge region could be eliminated and thereby reducing losses.

The design was carried out at relatively low relaxation factors due to the presence of small transonic regime near the leading edge of the airfoil which led to, relatively slow but stable design environment. After 920 design iterations the target Cp distribution was reached and Fig. 4.9a shows the initial, target and design Cp distributions. It is seen that the leading edge peak was reduced sufficiently and almost matches with the target. The small deviation could be attributed to retaining the shape of the leading edge which is enforced as a constraint in the first couple of percent. However, the leading edge did change its orientation so as to match the target. As expected the area and magnitude of separation is reduced, as seen in Fig. 4.10. The original and designed airfoil geometry are shown in Fig. 4.9b. The design and original values of c_l and c_d given in Table 4.8, show an increase in c_l and a decrease in c_d.

Since an angle of attack of 12° can be considered as off-design condition, steady state analysis of the redesigned airfoil was carried out at angles of attack varying from 0° to 14° in steps of 2°. The outcome of this in comparison with the original NACA 2412 airfoil is shown in Fig. 4.11. It is noticed that the performance of airfoil went down at lower angles of attack. This can be attributed to the fact that the redesign

was carried out higher angle of attack and thereby increasing the performance in the nearby range. To overcome this phenomenon, the dual point redesign is carried out as detailed in the last section of this chapter.

4.4. Redesign of RAE 2822 airfoil in transonic regime

The objective of this redesign case is to show that the inverse methodology can be implemented in cases of strong shock. RAE 2822 airfoil has been taken as the test case for this example. Test case 6 of section A-6 AGARD AR 138 has been chosen as the design condition (Mach no. = 0.725, AOA = 2.92 Degrees, Re = 6.5 millions). A strong shock is found between 50 and 60 percent chord. The Mach contour for RAE 2822 for the design flow field is shown in Fig. 4.12. Target Cp is chosen such that the shock is moved a small distance downstream of the present location with an intension of reducing the shock strength and hence reducing the wave drag. Design was started with the fully converged solution of the RAE 2822 airfoil under the given flow conditions. After 530 design steps the L_2 norm of grid displacements went down to 2×10^{-4}. Fig. 4.13 gives the sketch of original, design and target Cps after the design process. It is seen that the design Cp is very close the target Cp and does not fall right on top of the target at certain locations. A possible interpretation of this difference has to do with the resulting airfoil curvature upstream of the shock. However, an experienced designer would be able to produce a more appropriate target pressure distribution in the shock region, and, the methodology would yield an airfoil shape corresponding to the desired distribution. The c_l and c_d values for the redesigned airfoil show a slight improvement in comparison with the original RAE 2822 airfoil, see Table 4.9. The designed airfoil geometry is compared with the original RAE 2822 airfoil in Fig. 4.14.

Table 4.9: Redesign of RAE 2822 airfoil: $M_{inf} = 0.725, AOA = 2.92°, Re = 6.5$ millions

Lift coefficient (c_l)		Drag coefficient (c_d)		Lift/Drag (c_l/c_d)	
*D*esign	Original	Design	Original	Design	Original
0.783	0.782	0.0109	0.0111	71.862	70.459

4.5. Redesign of a multi-element airfoil

High lift devices have been under study for a long time. Minor changes in the orientation and (or) gap between the different elements could vary the performance by a considerable amount and hence designing them poses a challenging task. The study performed here is only to demonstrate the capability of the inverse design method that has been extended to accommodate the multi-element system.

The redesign of the NLR 7301 airfoil with a trailing edge flap was considered. The geometric configuration used in this case is that of a trailing flap with a 2.6 percent gap. The mesh is composed of a structured O/C grid around both the main element and trailing edge flap so as to resolve the boundary layer and to capture part of the wake and later the rectangles were cut into two triangles based on minimum area to minimize skewness. The distance of the first layer from the wall is such that the $y^+ \leq 1$ in both elements. The rest of the domain was meshed with unstructured mesh using Delaunay triangulation. The geometry and experimental data used for comparison are given in case A-9 of AGARD AR-303 [35]. For validation of the setup, the flow was simulated at AOA of 13.1°, Mach number of 0.185 and Reynolds number of 2.51 millions. Fig. 4.15 shows the numerical and experimental Cp distributions which are in good agreement.

For the inverse procedure, the Mach number is higher than the validation case and analysis was carried out at free stream conditions of Mach number 0.4, AOA of 3° and Reynolds number of 2 millions. The target Cp on the main element was intended such that the flow had more acceleration on the suction surface so as to increase the

Table 4.10: Redesign of multi element airfoil: $M_{inf} = 0.40, AOA = 3°, Re = 2.51$ millions

Lift coefficient (c_l)		Drag coefficient (c_d)		Lift/Drag (c_l/c_d)	
*D*esign	Original	Design	Original	Design	Original
2.262	2.165	0.0371	0.0424	60.75	51.07

lift. Note that the design procedure was applied to the main element only. Suction surface pressure and thickness distributions were specified and the target Cp was achieved in about 950 design steps; Fig. 4.16 shows the initial, target and design Cp distributions. Care was taken so as to ensure that there is no mesh tangling as the mesh movement is different in different sections of the domain due to which transition zones were defined so as to ensure even and smooth mesh movement. The initial and design airfoil geometries are shown in Fig. 4.17. It is seen that there is no change near the trailing edge of the main airfoil and the flapped section and thereby the original gap between the main element and flap was maintained. Design values of both c_l and c_d reflect an improvement over the original ones, moreover, as shown in Table 4.10 L/D is increased by 20 percent.

The redesign in this case involved the main element only, however, the methodology can accommodate the redesign of three or four element airfoil having both leading edge slat and trailing edge flap which mainly contribute to c_{lmax} and high lift respectively.

4.6. Dual-point design

The cases discussed in previous sections focussed on redesigning airfoils at the design point. It is also noted that the inverse design concept was conceived to redesign airfoils at a single design condition. The inverse design performed in this section involves the redesign of an airfoil taking into account two design conditions simultaneously.

NACA 2412 described in previous section with AOA of 12°, Mach of 0.39 and

Table 4.11: Dual point design of NACA 2412 airfoil - Design condition 1: $M_{inf} = 0.39, AOA = 12°, Re = 2$ millions

Lift coefficient (c_l)		Drag coefficient (c_d)		Lift/Drag (c_l/c_d)	
*D*esign	Original	Design	Original	Design	Original
1.431	1.250	0.0430	0.0517	33.28	24.18

Table 4.12: Dual point design of NACA 2412 airfoil - Design condition 2: $M_{inf} = 0.60, AOA = 4°, Re = 4$ millions

Lift coefficient (c_l)		Drag coefficient (c_d)		Lift/Drag (c_l/c_d)	
*D*esign	Original	Design	Original	Design	Original
0.849	0.747	0.0121	0.0113	69.63	65.99

Reynolds number of 2 millions was chosen as the first design point and the one described with an AOA of 4°, Mach of 0.6 and Reynolds number of 4 millions was chosen as the second design point. The first design point can be interpreted as the take-off condition and the second to the cruise condition. Following the flow chart given for multi-point design in Chapter 3 namely Fig. 3.4, two target Cps at the respective design conditions are given. The values given to the design weights are $w_1 = 0.75$ and $w_2 = 0.25$, in other words the off design point is given more weight than the cruise condition point. It is noted that since design is taking place at two points simultaneously with higher weight of one over the other, the target Cp corresponding to the lower weight may not be completely attained. Figure 4.18 shows the initial, target and design Cp distribution at design points 1 and 2. The initial and final airfoil geometries are shown in Fig. 4.19. The comparison of c_l and c_d values at both design conditions are given in Tables 4.11 and 4.12. Steady state analysis is performed on the redesign airfoil for angle of attack ranging from 0° to 16° for both the design conditions and the comparison of the performance parameters are shown in Fig. 4.20 and 4.21.

The reverse case, i.e. where weighting design condition 2 more than condition 1

has also been carried out. It is noted that no matter what the value of the weighting factors is, design condition 1 always dominates due to the values of Cp which are much higher compared with condition 2. Based on the above results, it seems that this method is best suited for designing airfoils at off-design conditions while keeping the performance at cruise conditions within the specified tolerance level.

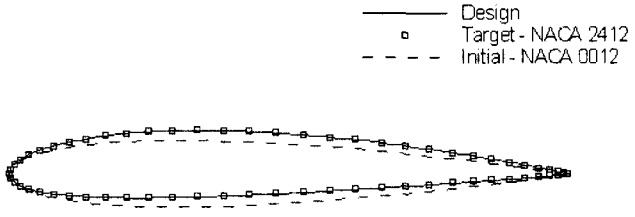

Figure 4.1: Validation Case 1: Initial, target and design airfoil geometry, design variables are p^+ and p^-

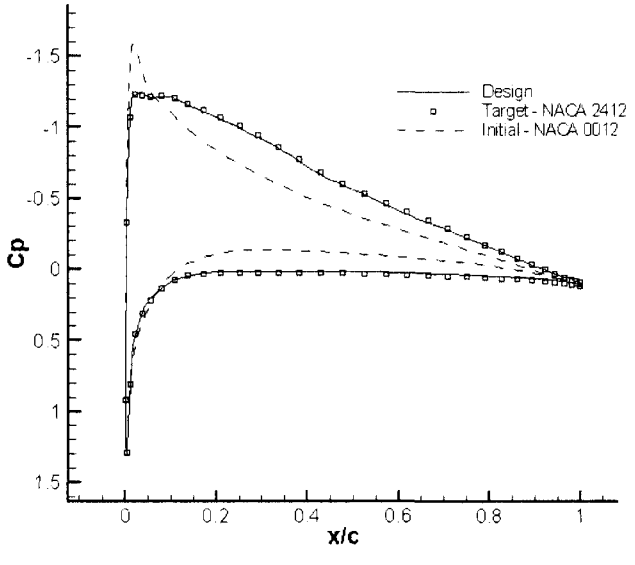

Figure 4.2: Validation Case 1: Initial, target and design Cp plot , design variables are p^+ and p^-

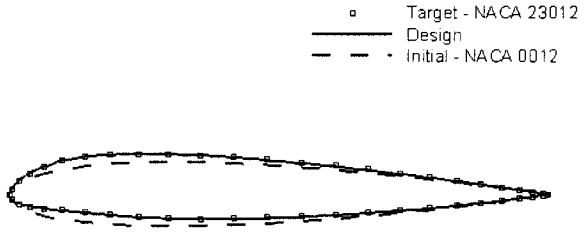

Figure 4.3: Validation Case 2: Initial, target and design airfoil geometry, design variables are p^- and thickness distribution

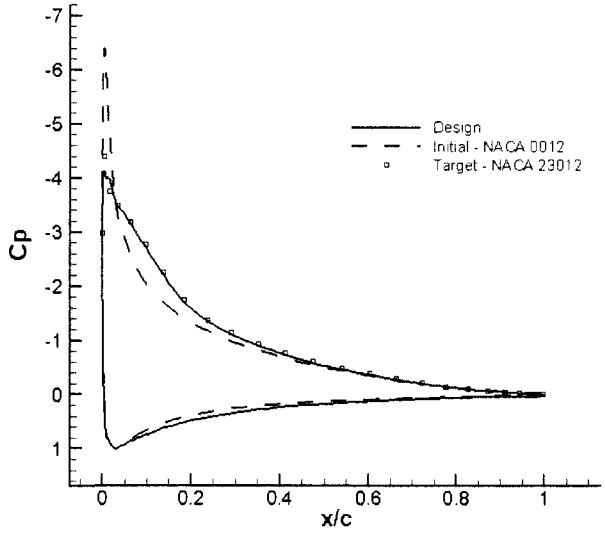

Figure 4.4: Validation Case 2: Initial, target and design Cp plot, design variables are p^- and thickness distribution

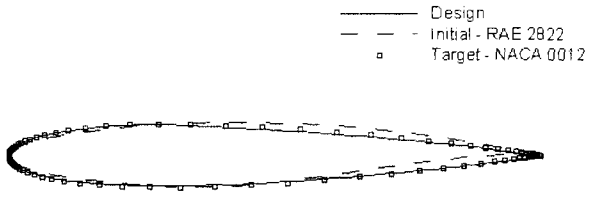

Figure 4.5: Validation Case 3: Initial, target and design airfoil geometry, design variables are p^+ and p^-

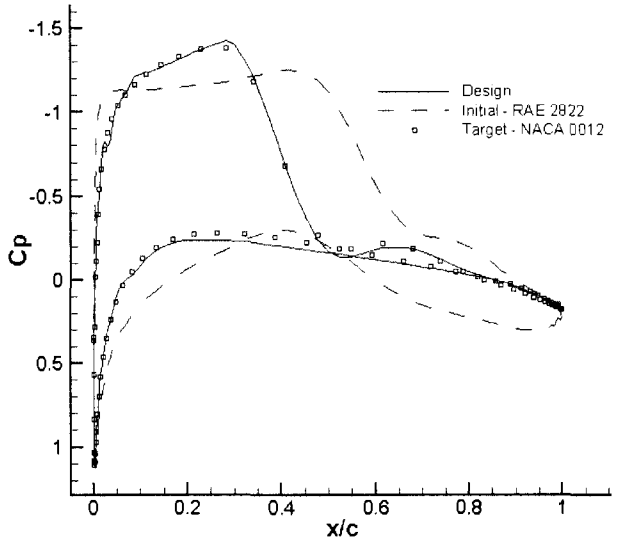

Figure 4.6: Validation Case 3: - Initial, target and design Cp plot, design variables are p^+ and p^-

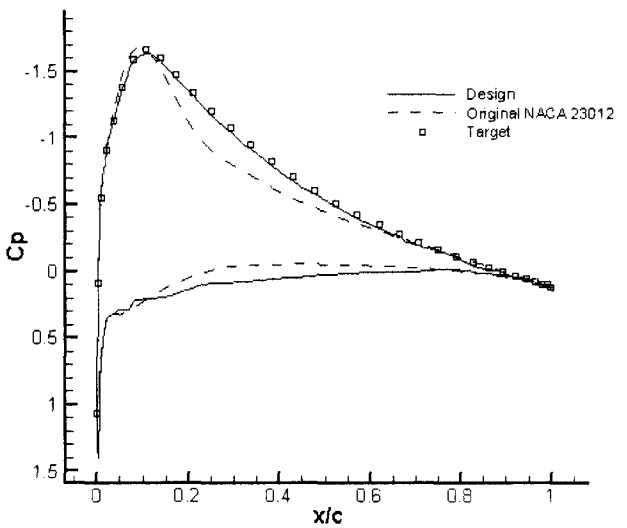

Figure 4.7: Redesign of NACA 23012: Original, target and design Cp distributions

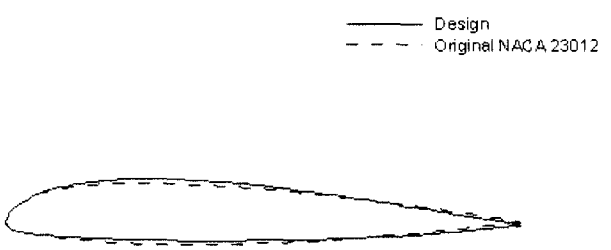

Figure 4.8: Redesign of NACA 23012: Original and redesigned airfoil geometry

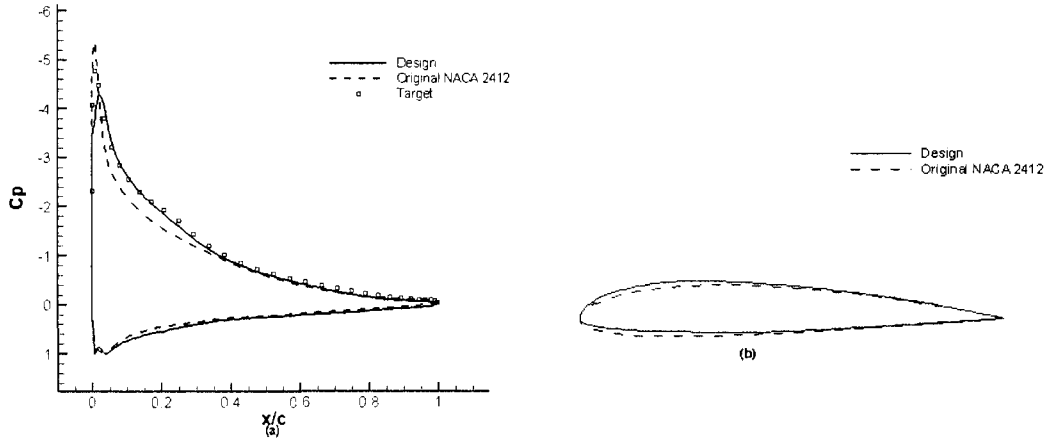

Figure 4.9: Redesign of NACA 2412: (a) Original, target and design Cp distributions, (b) Original and redesigned airfoil geometry

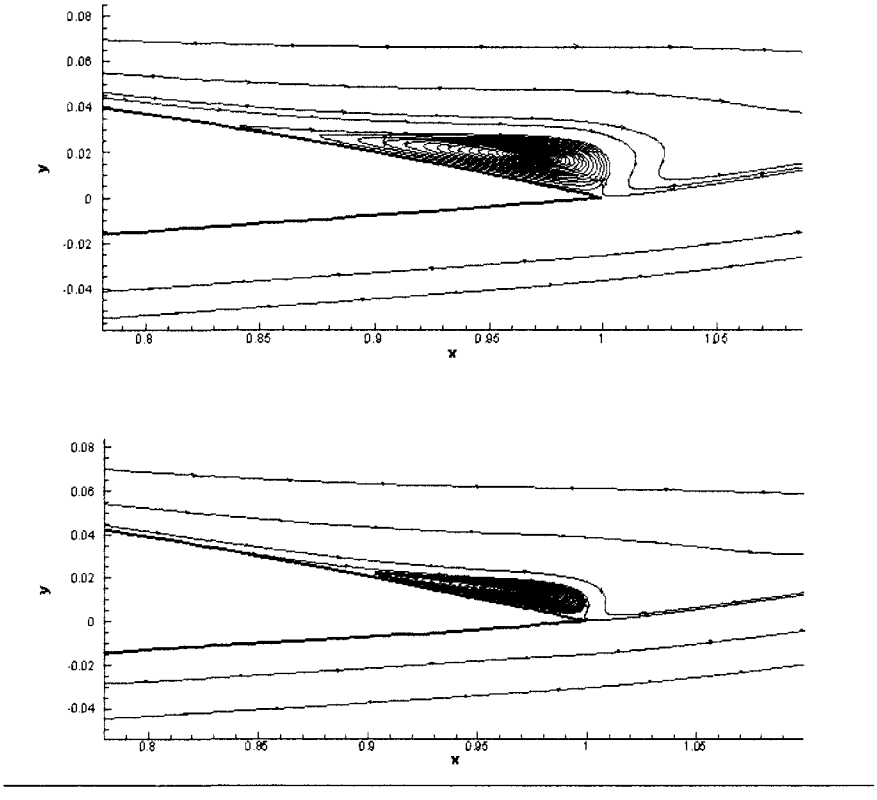

Figure 4.10: Redesign of NACA 2412: Recirculation zone on suction surface: Top-Initial, Bottom-Redesigned

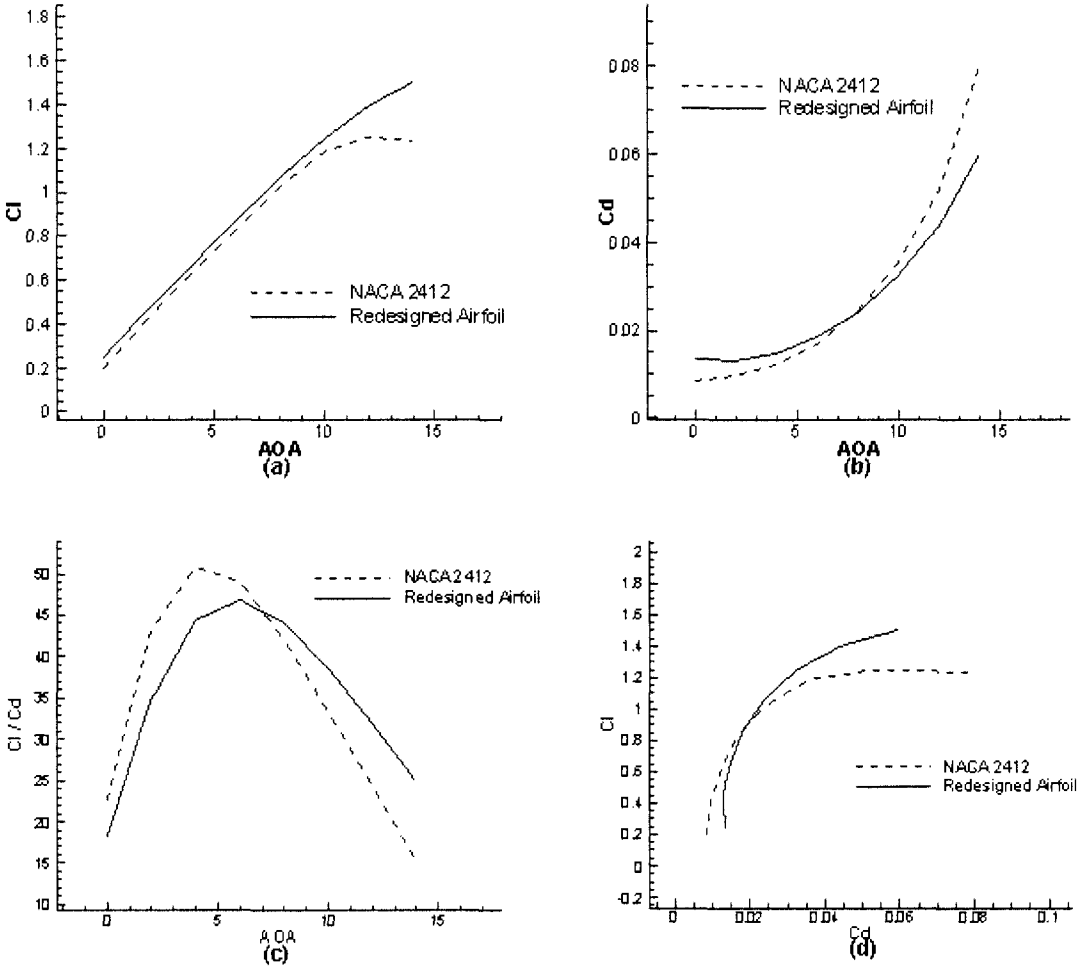

Figure 4.11: Redesign of NACA 2412: (a)c_l plot, (b)c_d plot, (c)c_l/c_d ratio, (d)Drag polar

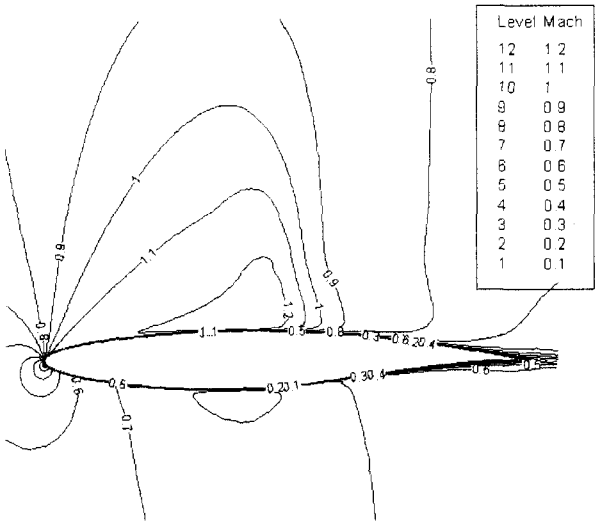

Figure 4.12: Mach contour of RAE 2822 airfoil: Mach=0.725, AOA=2.92°, Re=2.5 millions

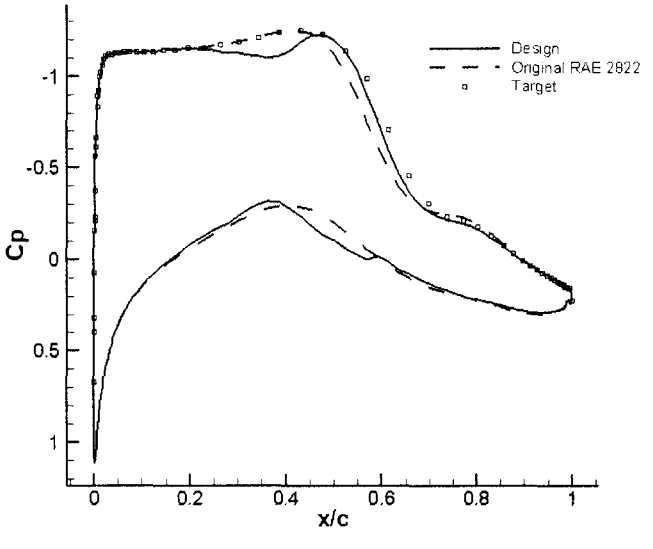

Figure 4.13: Redesign of RAE 2822: Original, target and design Cp distributions

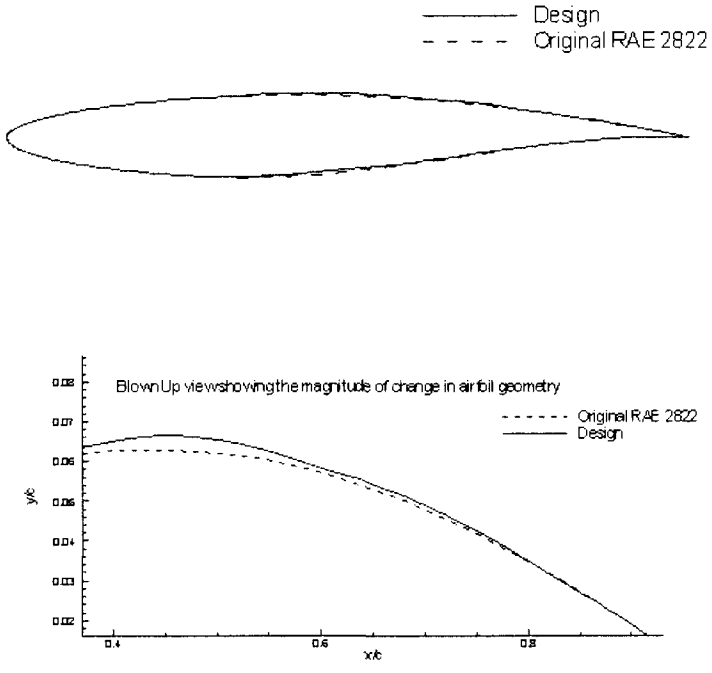

Figure 4.14: Redesign of RAE 2822: Original and redesigned airfoil geometry

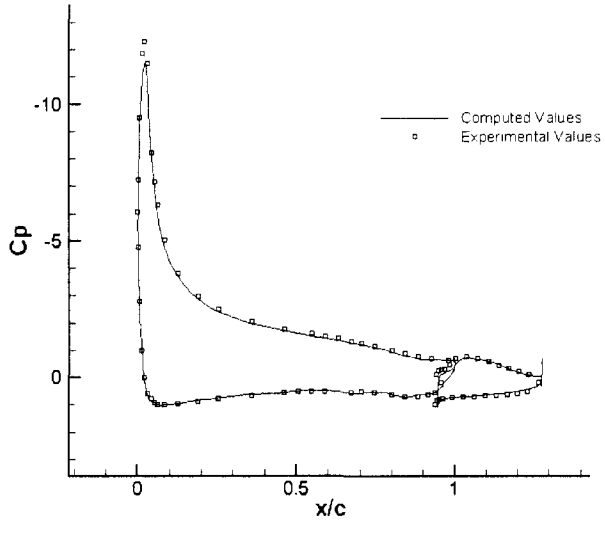

Figure 4.15: Pressure coefficient for NLR 7301 with trailing edge flap: Design conditions: M=0.185, Re=2.51 millions, AOA=13.1°

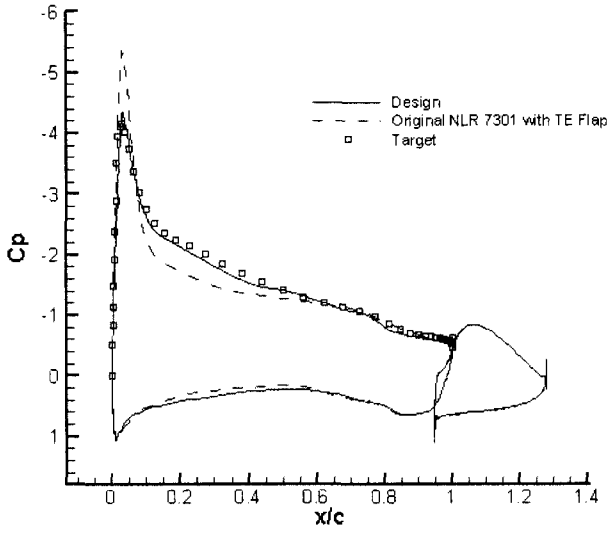

Figure 4.16: Redesign of NLR 7301: Original, target and design Cp distributions

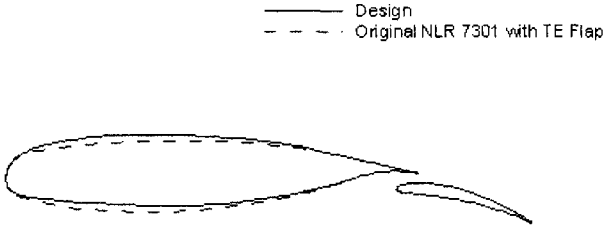

Figure 4.17: Redesign of NLR 7301: Original and redesigned airfoil geometry

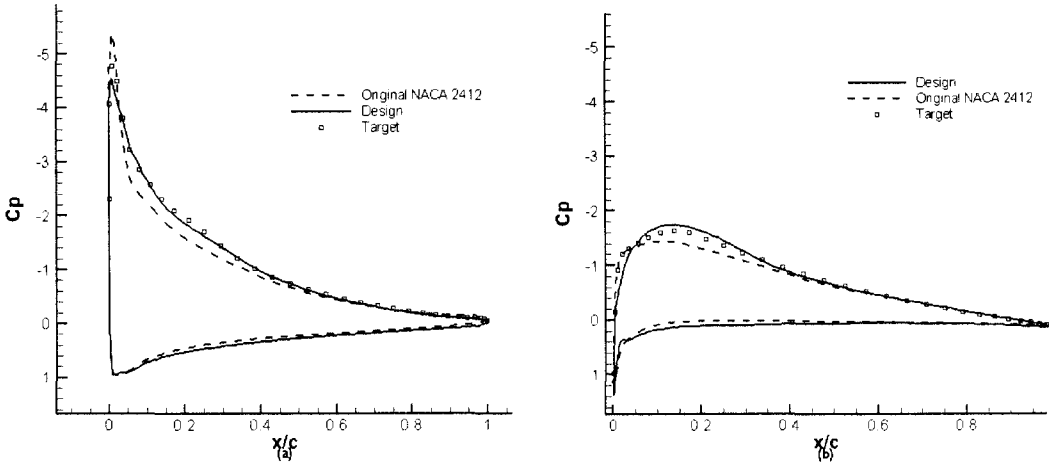

Figure 4.18: Dual-point design: Cp distributions (a) Design condition 1, (b) Design condition 2

Figure 4.19: Dual-point design: Original and redesigned airfoil geometry

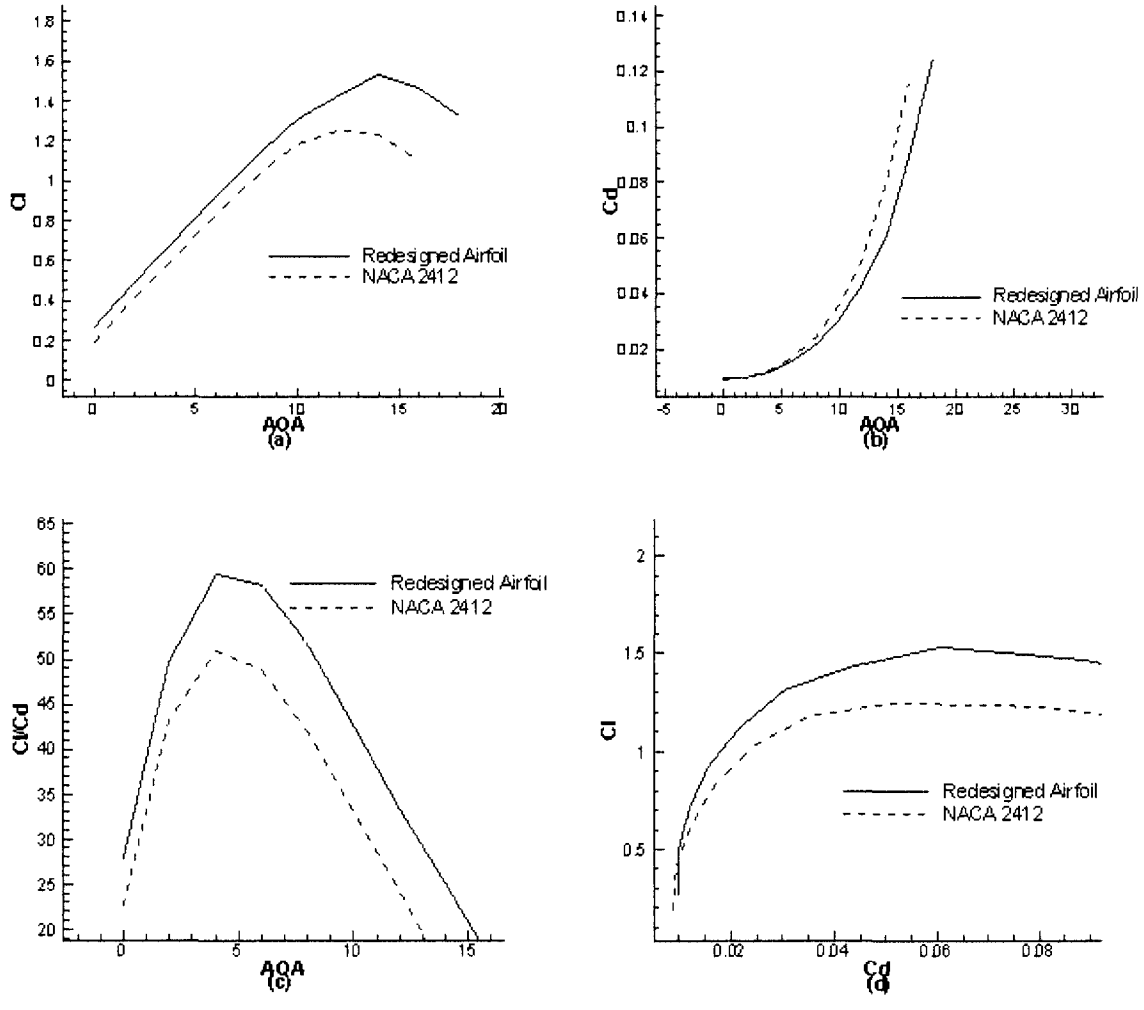

Figure 4.20: Dual-point design: Design condition 1: (a)c_l plot, (b)c_d plot, (c)c_l/c_d ratio, (d)Drag polar

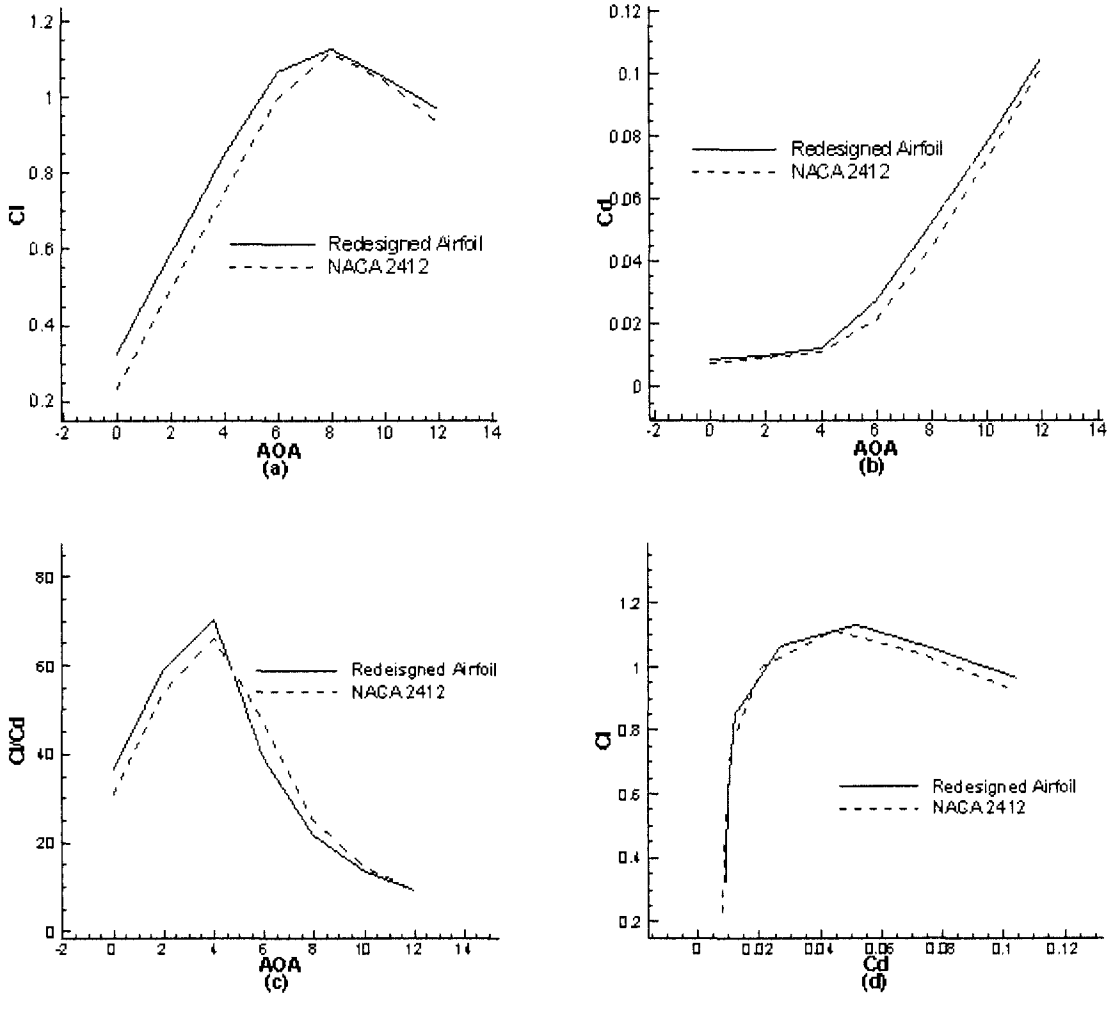

Figure 4.21: Dual-point design: Design condition 2: (a)c_l plot, (b)c_d plot, (c)c_l/c_d ratio, (d)Drag polar

Chapter 5

Conclusion

5.1. Summary

An aerodynamic inverse design method was successfully developed for 2D external flow, where the Cp distribution on the airfoil surfaces or the Cp^- and thickness distributions were the design variables. A virtual wall velocity was calculated from the difference between the target and current Cp distributions and was used to modify the airfoil geometry. The problem was solved in time accurate fashion which contributed to convergence acceleration as temporal errors were eliminated.

The method was initially validated and was later applied to a few redesign cases. The first redesign case involved performance improvement in terms of L/D. Other cases involved the redesign of an airfoil experiencing large separation, and an airfoil in transonic flow regime experiencing a shock. The improvement of performance in the second and third cases show the robustness of the method and its ability to work in the presence of separated flows and flows with shocks. The fourth redesign case is that of a multi-element airfoil where the main element was redesigned while the flap was run in analysis mode. The last design case demonstrated the flexibility of the method in dual and multi-point design where an airfoil is inversely designed at 2 or

more design conditions simultaneously.

5.2. Future work

- The results obtained in this thesis show that the method is successful in re-designing airfoils in 2D viscous flow. An optimizer tool could also be added in as a module to get the target pressure distribution based on criteria like maximum L/D ratio at a given condition.

- The next major step is to extend the inverse method to three dimensional flow, where many challenges will have to be addressed. For example, what is 'good' in terms of pressure distribution over a wing? How to deal with the wing tip region? How about the design constraints? Dual and multi-point design, is there a better way of implementing them in 3D flow situations?

Bibliography

[1] G. S. Dulikravich, "Aerodynamic shape design and optimization: Status and trends," *Journal of Aircraft*, vol. 29, 1992.

[2] M. J. Lighthill, "A new method of two-dimensional aerodynamic design," *Aeronautical Research Council*, 1945.

[3] G. B. McFadden, "An artificial viscosity method for the design of supercritical airfoils," *New York University Report*, 1979.

[4] P. R. Garabedian and D. G. Korn, "Numerical design of transonic airfoils," *Proc. SYNSPADE, Hubbard B., ed., Academic Press*, pp. 253–271, 1971.

[5] J. L. Tranen, "A rapid computer aided transonic airfoil design method," *AIAA paper*, 1974.

[6] P. A. Henne, "An inverse transonic wing design method," *Journal of Aircraft*, vol. 18, 1981.

[7] P. R. Garabedian and G. B. McFadden, "Computational fluid dynamics of airfoils and wings," *Proc. of Symposium on Transonic, Shock, and Multi-Dimensional Flows*, pp. 1–16, 1981.

[8] N. Hirose, S. Takanashi, and N. Kawai, "Transonic airfoil design procedure utilizing a navier-stokes analysis code," *AIAA*, vol. 25, no. 3, pp. 353–359, 1987.

[9] M. Giles and M. Drela, "Two dimensional transonic aerodynamic design method," *AIAA Journal*, vol. 25(9), pp. 1199–1205, 1987.

[10] J. B. Malone, J. C. Narramore, and L. N. Sankar, "Airfoil design method using the navier-stokes equations," *Journal of Aircraft*, vol. 28, no. 3, pp. 216–224, 1991.

[11] A. Gopalarathnam and M. S. Selig, "Multipoint inverse method for multielement airfoil design," *Journal of Aircraft*, vol. 35, no. 3, pp. 398–404, 1998.

[12] A. Gopalarathnam and M. S. Selig, "Low-speed natuaral-laminar-flow airfoils: Case study in inverse airfoil design," *Journal of Aircraft*, vol. 38, no. 1, pp. 57–63, 2001.

[13] M. S. Selig and M. D. Maughmer, "Multipoint inverse airfoil design method based on conformal mapping," *AIAA*, vol. 30, no. 5, pp. 1162–1170, 1992.

[14] M. S. Selig and M. D. Maughmer, "Generalized multipoing inverse airfoil design," *AIAA*, vol. 30, no. 11, pp. 2618–2625, 1992.

[15] A. Gopalarathnam and J. K. Jepson, "Inverse design of adaptive airfoils with aircraft performance considerations," *Journal of Aircraft*, vol. 42, 2005.

[16] H. J. Kim, C. Kim, and O. H. Rho, "Multipoint inverse design method for transonic wings," *Journal of Aircraft*, vol. 36, no. 6, pp. 941–947, 1999.

[17] W. E. Milholen-II, "Efficient inverse aerodynamics design meghod for subsonic flows," *Journal of Aircraft*, vol. 38, no. 5, pp. 918–923, 2001.

[18] K. Daneshkhah and W. Ghaly, "Aerodynamic inverse design for viscous flow in turbomachinery blading," *AIAA Journal of Propulsion and Power*, vol. 23, no. 4, pp. 814–820, 2007.

[19] K. Daneshkhah and W. Ghaly, "An inverse blade design method for subsonic and transonic viscous flow in compressors and turbines," *Journal of Inverse Problems in Science and Engineering*, vol. 14, no. 3, pp. 211–231, 2006.

[20] K. Daneshkhah and W. Ghaly, "Redesign of a highly loaded transonic turbine nozzle blade using a new viscous inverse design method," *ASME paper GT2007-27430*, 2007.

[21] B. Baldwin and H. Lomax, "Thin layer approximation and algebraic model for separated turbulent flows," *AIAA Paper 78-257*, 1978.

[22] D. Mavripilis, "Turbulent flow calculations using unstructured and adaptive meshes," *International Journal for Numerical Methods in Fluids*, vol. 91, no. 13, pp. 1131–1152, 1991.

[23] D. Mavriplis, A. Jameson, and L. Martinelli, "Multigrid solution of the navier stokes equations on triangular meshes," *AIAA Paper 89-0120*, 1989.

[24] I. Demirdzic and M. Peric, "Space conservation law in finite volume calculations of fluid flow," *International Journal for Numerical Methods in Fluids*, vol. 8, pp. 1037–1050, 1988.

[25] I. FLUENT, "Fluent 6.1 documentation," *Manual*, 2008.

[26] C. Hirsh, *Numerical Computation of Internal and External Flows*. Wiley-Interscience, 1994.

[27] T. Cebeci, J. P. Shao, F. Kafyeke, and E. Laurendeau, *Computational Fluid Dynamics for Engineers*. Springer, 2005.

[28] A. Demeulenaere, O. Leonard, and V. Braembussche, "A two-dimensional navier-stokes inverse solver for compressor and turbine blade design," *Proc. Inst. Mech. Eng. Part A, 211*, pp. 299–307, 1997.

[29] K. Daneshkhah, "Aerodynamic inverse design of turbomachinery blading in two-dimensional viscous flow," *Ph.D. Thesis, Concordia University, Department of Mechanical Engineering*, 2007.

[30] A. A. Hirt C.W. and C. J.L., "An arbitrary lagrangian-eulerian computing method for all flow speeds," *Journal of Computational Physics*, vol. 14, 1974.

[31] W. Mangler, "Die berechunung eines traflugelprofiles mit vorgeschriebener druckverteilung," *Jahrbuch der Deutschen Luftfahrtanschung*, 1938.

[32] G. Volpe and R. E. Melnik, "The design of transonic aerofoils by a well-posed inverse method," *International Journal for Numerical Methods in Engineering*, vol. 22, pp. 341–361, 1986.

[33] N. Gregory and P. G. Wilby, "Npl 9615 and naca 0012 a comparison of aerodynamic data," *Ministry of Defence, Aeronautical Research Council*, 1973.

[34] J. J. Thibert, M. Grandjacques, and L. H. Ohman, "Experimental data base for computer program assessment," *AGARD-AR-138*, 1979.

[35] B. van den Berg and J. H. M. Gooden, "A selection of experimental test cases for the validation of cfd codes," *AGARD-AR-303, Volume II*, 1994.

[36] D. R. Lindquist, "A comparison of numerical schemes on triangular and quadrilateral meshes," *M. S. Thesis, Massachusetts Institute of Technology, Department of Aeronautics and Astronautics*, 1988.

[37] D. Holmes and S. Connel, "Solution of 2-d navier-stokes equations on unstructured adaptive meshes," *AIAA Paper 89–1932*, 1989.

[38] A. Smith and T. Cebeci, "Numerical solution of the turbulent boundary layer equations," *Douglas aircraft division report DAC 33735*, 1967.

Appendix A

Flow Solver Details

In this appendix, the numerical implementation of the flow solver is detailed. The governing equations are discretized in space using the cell-vertex finite volume of Jameson scheme and explicit Runge-Kutta tile stepping is used to march to a steady state solution. For the turbulence closure algebraic Baldwin-Lomax turbulence model is used.

A.1. Integration to steady state

The discretization of the spatial derivatives without the grid velocities transforms Eq. 2.1 into the set of coupled ordinary differential equations

$$\Omega_i \frac{dU_i}{dt} + [Q(U_i) - D(w_i)] = 0 \quad i = 1, 2, 3, ..., n \tag{A.1}$$

where n is the number of mesh nodes. The residual $Q(U)$ represent the discrete approximation to the convective fluxes. $D(U)$ represents the dissipative and body force terms, i.e. the discrete approximation to the viscous fluxes, the artificial dissipation terms as well as the quasi 3-D related source term. These equations are integrated in

pseudo-time using a five-stage hybrid time-stepping scheme given by

$$\begin{aligned}
U^{(0)} &= U^n \\
U^{(1)} &= U^{(0)} - \alpha_1 \frac{\Delta t}{\Omega} \left[Q(U^{(0)}) - D_0 \right] \\
U^{(2)} &= U^{(0)} - \alpha_2 \frac{\Delta t}{\Omega} \left[Q(U^{(1)}) - D_1 \right] \\
U^{(3)} &= U^{(0)} - \alpha_4 \frac{\Delta t}{\Omega} \left[Q(U^{(2)}) - D_2 \right] \\
U^{(4)} &= U^{(0)} - \alpha_4 \frac{\Delta t}{\Omega} \left[Q(U^{(3)}) - D_3 \right] \\
U^{(5)} &= U^{(0)} - \alpha_5 \frac{\Delta t}{\Omega} \left[Q(U^{(4)}) - D_4 \right] \\
U^{n+1} &= U^{(5)}
\end{aligned} \tag{A.2}$$

where

$$\begin{aligned}
D_0 &= D_1 = D(w^{(0)}) \\
D_2 &= D_3 = \beta\, D(w^{(2)}) + (1-\beta)\, D(U^{(0)}) \\
D_4 &= \gamma\, D(U^{(4)}) + (1-\gamma)\, D(w^{(2)})
\end{aligned} \tag{A.3}$$

U^n represents the value of the solution vector at the nth time step and $U^{(q)}$ represents the values at the qth stage within a time step. The dissipative operator $D(U)$ is evaluated only at the first, third, and fifth stages of the scheme, and is employed to construct the subscripted D_q operator which represents a linear combination of present and previous evaluation of $D(U)$. This scheme represents a particular case of a large class of multi-stage time-stepping schemes where the coefficients are chosen in order to maintain good stability properties when the viscous terms are dominant, and to ensure large damping of high-frequency errors. The values of these coefficients are taken as

$$\beta = 0.56 \quad \gamma = 0.44$$

and

$$\alpha_1 = 1/4 \quad \alpha_2 = 1/6 \quad \alpha_3 = 3/8 \quad \alpha_4 = 1/2 \quad \alpha_5 = 1$$

A.2. Space discretization

The flux calculation is carried out based on Jameson scheme on a fully unstructured mesh [36]. If n is the number of cells surrounding the node 1 thus forming the control volume. For the control volume shown in figure A.1 $n = 6$. The flux used in the equation A.1 namely (Q(U) - D) is computed as follows.

The contribution of cell A to the flux at nodes 1, 2 and 3 are the same. Thus

$$flux_{1A} = flux_{2A} = flux_{3A} = flux_A$$

where

$$\begin{aligned} flux_A = \frac{1}{2}[&-(F_2 + F_1)(y_2 - y_1) + (G_2 + G_1)(x_2 - x_1) \\ &-(F_3 + F_2)(y_3 - y_2) + (G_3 + G_2)(x_3 - x_2) \\ &-(F_1 + F_3)(y_1 - y_3) + (G_1 + G_3)(x_1 - x_3)] \end{aligned} \tag{A.4}$$

which reduces to

$$\begin{aligned} flux_A = \frac{1}{2}[&-F_1(y_2 - y_3) + G_1(x_2 - x_3) \\ &-F_2(y_3 - y_1) + G_2(x_3 - x_1) \\ &-F_3(y_1 - y_2) + G_3(x_1 - x_2)] \end{aligned} \tag{A.5}$$

The flux at node 1 is the sum of all the contributions from n surrounding cells.

$$flux_1 = flux_{1A} + flux_{1B} + ... + flux_{1n}$$

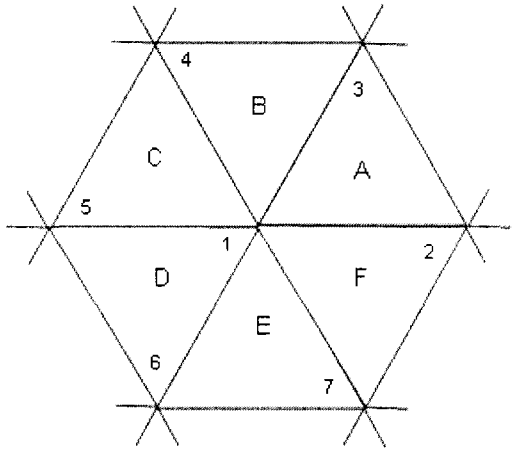

Figure A.1: Triangular cells surrounding node 1 with control volume

A.3. Artificial dissipation

In principle, the physical viscous terms of the Navier-Stokes equations are capable of providing the numerical scheme with the dissipative property necessary for stability and capturing discontinuities. However, for high Reynolds-number flows, this can only be achieved by resorting to extremely small mesh spacing throughout the domain. Thus, in practice, it is necessary to introduce artificial dissipative terms to maintain stability in the essentially inviscid portion of the flow field, and to efficiently capture discontinuities. These additional dissipative terms must be carefully constructed to ensure that the accuracy of the scheme is preserved both in the inviscid region of the flow field where the convective terms dominate, as well as in the boundary layer and wake region where the artificial dissipation terms must be much smaller than the physical viscous terms. Previous Navier-stokes solutions on highly stretched meshes have demonstrated the need for different scaling of the artificial dissipation

terms in the streamwise and normal directions within the regions of viscous flow. However, for unstructured meshes, directional scaling is significantly more difficult to achieve since no mesh coordinate line exist. In fact, unstructured meshes have traditionally been considered to be truly multi-dimensional isotropic constructions with no preferred direction. However, as stated perviously, the efficient solution of high-Reynolds-number viscous flows requires the meshes with highly stretched elements in the boundary layer and wake region, since the physical phenomena are highly directional in nature. For such meshes, even in the unstructured case, a direction and a magnitude of the stretching can be defined for each mesh point. This stretching vector, denoted as $\mathbf{s}$ need not necessarily line up with any of the mesh edges. If the mesh is directly derived from structured quadrilateral mesh by splitting each quadrilateral into two triangles, the stretching magnitude and direction may be taken as the aspect ratio and the major axis of the generating quadrilateral element for each triangular element respectively. In more general cases, the generation of directionally stretched unstructured mesh requires the definition of local stretching factors throughout the flow field. These can in turn be used to scale the dissipation terms. It is important to note that these stretching vectors represent grid metrics which do not depend on the flow solution.

The artificial dissipation operators on unstructured meshes has previously been constructed as a blend of an undivided pseudo-Laplacian, proposed by Holmes and Connel [37], and biharmonic operator in the flow field. The pseudo-Laplacian for a node is given by

$$\nabla^2(U_i) = \sum_{k=1}^{n} w_{k,i}(U_k - U_i) \tag{A.6}$$

where k represent all neighbors of node i. The weights $w_{k,i}$ are chosen such that the pseudo-Laplacian of a linear function will be zero, as would be the case for true

Laplacian. These weights are defined as

$$w_{k,i} = 1 + \Delta w_{k,i} \tag{A.7}$$

where $\Delta w_{k,i}$ are computed as

$$\Delta w_{k,i} = \chi_{x,i}(x_k - x_i) + \chi_{y,i}(y_k - y_i) \tag{A.8}$$

where

$$\begin{aligned} \chi_{x,i} &= \frac{(I_{xy}R_y - I_{yy}R_x)_i}{(I_{xx}I_{yy} - I_{xy}^2)_i} \\ \chi_{y,i} &= \frac{(I_{xy}R_x - I_{xx}R_y)_i}{(I_{xx}I_{yy} - I_{xy}^2)_i} \end{aligned} \tag{A.9}$$

in the above equations R and I represents the first and second moment of inertia of the control volume in each coordinate direction, that is:

$$\begin{aligned} R_{x,i} &= \sum_{k=1}^{n}(x_k - x_i) \\ R_{y,i} &= \sum_{k=1}^{n}(y_k - y_i) \end{aligned} \tag{A.10}$$

and

$$\begin{aligned} I_{xx,i} &= \sum_{k=1}^{n}(x_k - x_i)^2 \\ I_{yy,i} &= \sum_{k=1}^{n}(y_k - y_i)^2 \\ I_{xy,i} &= \sum_{k=1}^{n}(x_k - x_i)(y_k - y_i) \end{aligned} \tag{A.11}$$

The biharmonic artificial viscosity term is formed by taking the pseudo-Laplacian of

∇w_i

$$\nabla^4 w_i = \sum_{k=1}^{n} (\nabla^2 w_k - \nabla^2 U_i) \tag{A.12}$$

Since the biharmonic operator may be viewed as a Laplacian of a Laplacian, the dissipation operator may be reformulated as a global undivided Laplacian operating on a blend of flow variables and their differences

$$D(U) = \Omega\alpha[U_{xx} + U_{yy}] \tag{A.13}$$

where

$$C = \kappa_2' U - \kappa_4 \nabla^2 U \tag{A.14}$$

In the above equations, Ω represent the area of the control volume, which is of the order Δx^2, and $\nabla^2 U$ denotes the undivided Laplacian of U. The first term in the above equation constitutes a relatively strong-order dissipation term which is necessary to prevent un-physical oscillations in the vicinity of a shock. This term must be turned off in regions of smooth flow. This is accomplished by evaluating κ'^2 at mesh point i as

$$(\kappa_2') = \kappa_2 \frac{\sum_{k=1}^{n} [p_k - p_i]}{\sum_{k=1}^{n} [p_k + p_i]} \tag{A.15}$$

Hence κ_2' is proportional to an undivided Laplacian of the pressure, which is constructed as a summation of the pressure differences along all edges meeting at node i. This construction has the required property of being of the order unity near a shock and small elsewhere. κ_2 is an empirically determined coefficient which is taken as 0 for subcritical flows, and as $1/2$ for transonic and supersonic flows.

A.3.1 Local time stepping

Convergence to the steady-state solution may be accelerated by sacrificing the time accuracy of the scheme, and advancing the equations at each mesh point in time by

the maximum permissible time step in that region, as determined by local stability analysis. Stability limitation due to both convective and diffusive characters of Navier-Stokes equations must be considered. The local time step is taken as

$$\Delta t = CFL \left(\frac{\Delta t_c \, \Delta t_d}{\Delta t_c + \Delta t_d} \right) \tag{A.16}$$

where CFL is the Courant number of the particular time-stepping scheme, and Δt_c and Δt_d represent the individual convective and viscous time-step limits respectively, the convective time-step limit for Euler equation on unstructured meshes is given by

$$\Delta t_c = \frac{\Omega}{\lambda_c} \tag{A.17}$$

where Ω denotes the area of the control volume and λ_c represents the maximum eigenvalue of the inviscid equations averaged around the boundary of the control volume, given by

$$\lambda = \sum_{e=1}^{n} |u_{AB} \Delta y_{AB} - v_{AB} \Delta x_{AB}| + c_{AB} \sqrt{\Delta x_{AB}^2 + \Delta y_{AB}^2} \tag{A.18}$$

The viscous time-step limit is taken as

$$\Delta t_d = K_d \frac{\Omega}{\lambda_d} \tag{A.19}$$

where K_d is an empirically determined coefficient which determines the relative importance of the viscous and inviscid time-step limits in the final expressions, and has taken as 0.25 in this work. λ_c and λ_d represent the maximum eigenvalue of the convective and diffusive operators, respectively, averaged about the boundary of the control volume, which for an unstructured mesh in discrete form is given by

$$\lambda_d = \frac{\gamma}{Re \, Pr \, \Omega} \sum_{e=1}^{n} \frac{\mu_{AB}}{\rho_{AB}} [\Delta x_{AB}^2 + \Delta y_{AB}^2] \tag{A.20}$$

where μ_{AB} and ρ_{AB} represent averaged values of viscosity and density along the outer edge AB of each element e.

A.3.2 Implicit residual smoothing

The stability range of the basic time-stepping scheme can be increased by implicitly smoothing the residuals. Thus, the original residuals R may be replaced by the smoothed residuals $\overline{R}$ by solving the implicit equations:

$$\overline{R}_i = R_i + \varepsilon \nabla^2 \overline{R}_i \tag{A.21}$$

at each mesh point i, where ε is the smoothing coefficient and $\nabla^2 \overline{R}_i$ represents the undivided Laplacian of the residuals which has been previously computed using the pseudo-Laplacian formulation and the geometrical weights, so that Eq. A.22 may be written as:

$$\overline{R}_i = \frac{R_i + \epsilon \sum_{j=1}^{n} w_{j,i} \overline{R}_j}{1 + \epsilon \sum_{j=1}^{n} w_{j,i}} \tag{A.22}$$

A.4. Dual time stepping scheme

For unsteady flow calculations, the time accuracy of the solution is obtained by means of a dual time stepping scheme, which is presented in this section. Equations A.1 can be discretized implicitly in time as follows

$$\frac{d}{dt}\left[U^{n+1}\Omega^{n+1}\right] + R(U^{n+1}) = 0 \tag{A.23}$$

where R is the sum of the three flux contributions, and the superscripts denote the time step of the calculation. If we discretize the time derivative term with the implicit

second order Gear scheme, we obtain:

$$\frac{3}{2\Delta t}\left[U^{n+1}\Omega^{n+1}\right] - \frac{2}{\Delta t}\left[U^{n}\Omega^{n}\right] + \frac{1}{2\Delta t}\left[U^{n-1}\Omega^{n-1}\right] + R(U^{n+1}) = 0 \qquad \text{(A.24)}$$

This equation for U^{n+1} is non-linear due to the presence of the $R(U^{n+1})$ term and cannot be solved directly. One must therefore resort to iterative methods in order to obtain the solution. The time integration of the discretized Navier-Stokes equations at each time step can then be considered as a modified pseudo-time steady-state problem with a slightly altered residual:

$$R^{*}(U) = \frac{3}{2\Delta t}\left[U\Omega^{n+1}\right] - \frac{2}{\Delta t}\left[U^{n}\Omega^{n}\right] + \frac{1}{2\Delta t}\left[U^{n-1}\Omega^{n-1}\right] + R(U) \qquad \text{(A.25)}$$

In this case, the vector of flow variables U which satisfies the equation $R^{*}(U) = 0$ is the $U^{(n+1)}$ vector we are looking for. In order to obtain this solution vector, we can reformulate the problem at each time step as the following modified steady-state problem in a fictitious time, t^{*}

$$\frac{dU}{dt^{*}} + R^{*}(U) = 0 \qquad \text{(A.26)}$$

to which one can apply the fast convergence techniques used for steady-state calculations. Applying this process repeatedly, one can advance the flow field solution forward in time in a very efficient fashion.

The time discretization of Eq. A.24 is fully implicit. However, when solved by marching in t^{*}, stability problems can occur when the stepping in the fictitious time t^{*} exceeds the physical one. This generally occurs in viscous calculations where core flow cells are much bigger than those close to solid walls. Based on a linear stability

analysis, the stepping in t^* must be less than Δt^*_{max} where

$$\Delta t^*_{max} = \min \left[\Delta t^* \, , \, \frac{2CFL^*}{3CFL} \, \Delta t \right] \tag{A.27}$$

After limiting the time step to Δt^*_{max}, the scheme becomes stable and the physical time step Δt can be safely chosen solely on the basis of the accuracy requirement.

Appendix B

Turbulence Modelling

A brief overview of Baldwin-Lomax turbulence model is given in this section. The Baldwin-Lomax turbulence model [21] was developed as a simple algebraic turbulence model for implementing with the Navier-Stokes code. This model is based on the widely used Cebeci -Smith boundary layer model [38] with modifications made to avoid the need to search the edge of boundary layer. This implementation is adopted here for reasons of computational inexpensiveness and its simplicity in implementation. Even though the model is algebraic, the model has demonstrated its superior accuracy and reliability for limited class of problems [22].

B.1. Description of the model

The model is based on a two layer eddy diffusivity formulation. The turbulent length scales must be determined by scanning profiles of flow variables at specified streamwise stations. Therefore additional measures need to be taken for unstructured meshes as the mesh points do not occur at regular streamwise locations. Thus, lines normal to the walls and viscous layers must be created additionally to the unstructured mesh and hence the background mesh comes into picture. Flow variables from the unstructured mesh (foreground mesh) need to be interpolated into the structured background mesh

in order that the turbulence length scales may be determined. The background mesh can be obtained by generating a structured hyperbolic mesh around the geometry. The normal mesh lines are terminated when they intersect a neighboring geometry. At each time step, the flow variables are interpolated into the background mesh where the turbulence length scales and in turn the eddy viscosities are calculated and the results are interpolated back to the foreground mesh.

The effective turbulent viscosity is taken as

$$\frac{\mu_t}{\mu_{ref}} = \mu_t^* = \begin{cases} (\mu_t^*)_{inner} & y^* < y^*_{crossover} \\ (\mu_t^*)_{outer} & y^*_{crossover} < y^* \end{cases} \tag{B.1}$$

where y^* is the dimensionless distance to the wall and $y^*_{crossover}$ is the minimum value of y^* at which $(\mu_t^*)_{inner} > (\mu_t^*)_{outer}$.

The inner formulation follows the Prandtl-Van Driest formula. Dropping the prescript * for clarity, the eddy viscosity coefficient in the inner layer is defined as

$$(\mu_t^*)_{inner} = \rho l^2 |\omega| \tag{B.2}$$

where

$$l = ky[1 - exp(\frac{-y^+}{A^+})] \tag{B.3}$$

is the turbulence length scale in the inner region, k is the model constant and $|\omega|$ is the magnitude of vorticity vector and y^+ is the dimensionless distance from the wall which is defined as

$$y^+ = \frac{\sqrt{\rho \tau y}}{\mu} \tag{B.4}$$

The eddy viscosity in the outer layer is defined as

$$(\mu_t^*)_{outer} = K \rho C_{cp} F_{Kleb} min \begin{cases} y_{max} F_{max} \\ C_{wk} y_{max} \frac{u_{diff}^2}{F_{max}} \end{cases} \tag{B.5}$$

where K and C_{cp} are model constants and quantities F_{max} and y_{max} are determined by the value and corresponding location of the maximum of the function

$$F(y) = y|\omega|[1 - exp(\frac{-y^+}{A^+})] \tag{B.6}$$

Due to the potential existence of spurious maxima in $F(y)$, the search of finding the maximum of the function is limited to within y^+ values of 100 and 4000. The Klebanoff intermittency factor F_{Kleb} is given by

$$F_{Kleb} = \frac{1}{1 + 5.5[\frac{C_{Kleb}y}{y_{max}}]^6} \tag{B.7}$$

Also, trnasition to turbulence can be modeled by setting a cut off value for the computed eddy viscosity. The suggested criterion is

$$\mu_t = 0 \quad if \quad \mu_{max} < C_{mutm} \tag{B.8}$$

The constant values are given by

$$\begin{aligned} A^+ = 26 \quad C_{cp} = 1.6 \quad C_{Kleb} = 0.3 \\ k = 0.4 \quad K = 0.0168 \quad C_{mutm} = 14 \end{aligned} \tag{B.9}$$